Study of the reactions $e^+e^- \to \pi^+\pi^-\pi^0\pi^0\pi^0$ and $\pi^+\pi^-\pi^0\pi^0\eta$ at center-of-mass energies from threshold to 4.35 GeV using initial-state radiation

J. P. Lees,[1] V. Poireau,[1] V. Tisserand,[1] E. Grauges,[2] A. Palano,[3] G. Eigen,[4] D. N. Brown,[5] Yu. G. Kolomensky,[5] M. Fritsch,[6] H. Koch,[6] T. Schroeder,[6] C. Hearty,[7a,7b] T. S. Mattison,[7b] J. A. McKenna,[7b] R. Y. So,[7b] V. E. Blinov,[8a,8b,8c] A. R. Buzykaev,[8a] V. P. Druzhinin,[8a,8b] V. B. Golubev,[8a,8b] E. A. Kozyrev,[8a,8b] E. A. Kravchenko,[8a,8b] A. P. Onuchin,[8a,8b,8c] S. I. Serednyakov,[8a,8b] Yu. I. Skovpen,[8a,8b] E. P. Solodov,[8a,8b] K. Yu. Todyshev,[8a,8b] A. J. Lankford,[9] J. W. Gary,[10] O. Long,[10] A. M. Eisner,[11] W. S. Lockman,[11] W. Panduro Vazquez,[11] D. S. Chao,[12] C. H. Cheng,[12] B. Echenard,[12] K. T. Flood,[12] D. G. Hitlin,[12] J. Kim,[12] Y. Li,[12] T. S. Miyashita,[12] P. Ongmongkolkul,[12] F. C. Porter,[12] M. Röhrken,[12] Z. Huard,[13] B. T. Meadows,[13] B. G. Pushpawela,[13] M. D. Sokoloff,[13] L. Sun,[13,†] J. G. Smith,[14] S. R. Wagner,[14] D. Bernard,[15] M. Verderi,[15] D. Bettoni,[16a] C. Bozzi,[16a] R. Calabrese,[16a,16b] G. Cibinetto,[16a,16b] E. Fioravanti,[16a,16b] I. Garzia,[16a,16b] E. Luppi,[16a,16b] V. Santoro,[16a] A. Calcaterra,[17] R. de Sangro,[17] G. Finocchiaro,[17] S. Martellotti,[17] P. Patteri,[17] I. M. Peruzzi,[17] M. Piccolo,[17] M. Rotondo,[17] A. Zallo,[17] S. Passaggio,[18] C. Patrignani,[18,‡] H. M. Lacker,[19] B. Bhuyan,[20] U. Mallik,[21] C. Chen,[22] J. Cochran,[22] S. Prell,[22] A. V. Gritsan,[23] N. Arnaud,[24] M. Davier,[24] F. Le Diberder,[24] A. M. Lutz,[24] G. Wormser,[24] D. J. Lange,[25] D. M. Wright,[25] J. P. Coleman,[26] E. Gabathuler,[26,*] D. E. Hutchcroft,[26] D. J. Payne,[26] C. Touramanis,[26] A. J. Bevan,[27] F. Di Lodovico,[27] R. Sacco,[27] G. Cowan,[28] Sw. Banerjee,[29] D. N. Brown,[29] C. L. Davis,[29] A. G. Denig,[30] W. Gradl,[30] K. Griessinger,[30] A. Hafner,[30] K. R. Schubert,[30] R. J. Barlow,[31,§] G. D. Lafferty,[31] R. Cenci,[32] A. Jawahery,[32] D. A. Roberts,[32] R. Cowan,[33] S. H. Robertson,[34a,34b] R. M. Seddon,[34b] B. Dey,[35a] N. Neri,[35a] F. Palombo,[35a,35b] R. Cheaib,[36] L. Cremaldi,[36] R. Godang,[36,¶] D. J. Summers,[36] P. Taras,[37] G. De Nardo,[38] C. Sciacca,[38] G. Raven,[39] C. P. Jessop,[40] J. M. LoSecco,[40] K. Honscheid,[41] R. Kass,[41] A. Gaz,[42a] M. Margoni,[42a,42b] M. Posocco,[42a] G. Simi,[42a,42b] F. Simonetto,[42a,42b] R. Stroili,[42a,42b] S. Akar,[43] E. Ben-Haim,[43] M. Bomben,[43] G. R. Bonneaud,[43] G. Calderini,[43] J. Chauveau,[43] G. Marchiori,[43] J. Ocariz,[43] M. Biasini,[44a,44b] E. Manoni,[44a] A. Rossi,[44a] G. Batignani,[45a,45b] S. Bettarini,[45a,45b] M. Carpinelli,[45a,45b,**] G. Casarosa,[45a,45b] M. Chrzaszcz,[45a] F. Forti,[45a,45b] M. A. Giorgi,[45a,45b] A. Lusiani,[45a,45c] B. Oberhof,[45a,45b] E. Paoloni,[45a,45b] M. Rama,[45a] G. Rizzo,[45a,45b] J. J. Walsh,[45a] L. Zani,[45a,45b] A. J. S. Smith,[46] F. Anulli,[47a] R. Faccini,[47a,47b] F. Ferrarotto,[47a] F. Ferroni,[47a,††] A. Pilloni,[47a,47b] G. Piredda,[47a,*] C. Bünger,[48] S. Dittrich,[48] O. Grünberg,[48] M. Heß,[48] T. Leddig,[48] C. Voß,[48] R. Waldi,[48] T. Adye,[49] F. F. Wilson,[49] S. Emery,[50] G. Vasseur,[50] D. Aston,[51] C. Cartaro,[51] M. R. Convery,[51] J. Dorfan,[51] W. Dunwoodie,[51] M. Ebert,[51] R. C. Field,[51] B. G. Fulsom,[51] M. T. Graham,[51] C. Hast,[51] W. R. Innes,[51,*] P. Kim,[51] D. W. G. S. Leith,[51] S. Luitz,[51] D. B. MacFarlane,[51] D. R. Muller,[51] H. Neal,[51] B. N. Ratcliff,[51] A. Roodman,[51] M. K. Sullivan,[51] J. Va'vra,[51] W. J. Wisniewski,[51] M. V. Purohit,[52] J. R. Wilson,[52] A. Randle-Conde,[53] S. J. Sekula,[53] H. Ahmed,[54] M. Bellis,[55] P. R. Burchat,[55] E. M. T. Puccio,[55] M. S. Alam,[56] J. A. Ernst,[56] R. Gorodeisky,[57] N. Guttman,[57] D. R. Peimer,[57] A. Soffer,[57] S. M. Spanier,[58] J. L. Ritchie,[59] R. F. Schwitters,[59] J. M. Izen,[60] X. C. Lou,[60] F. Bianchi,[61a,61b] F. De Mori,[61a,61b] A. Filippi,[61a] D. Gamba,[61a,61b] L. Lanceri,[62] L. Vitale,[62] F. Martinez-Vidal,[63] A. Oyanguren,[63] J. Albert,[64b] A. Beaulieu,[64b] F. U. Bernlochner,[64b] G. J. King,[64b] R. Kowalewski,[64b] T. Lueck,[64b] I. M. Nugent,[64b] J. M. Roney,[64b] R. J. Sobie,[64a,64b] N. Tasneem,[64b] T. J. Gershon,[65] P. F. Harrison,[65] T. E. Latham,[65] R. Prepost,[66] and S. L. Wu[66]

(*BABAR* Collaboration)

[1]*Laboratoire d'Annecy-le-Vieux de Physique des Particules (LAPP), Université de Savoie, CNRS/IN2P3, F-74941 Annecy-Le-Vieux, France*
[2]*Universitat de Barcelona, Facultat de Fisica, Departament ECM, E-08028 Barcelona, Spain*
[3]*INFN Sezione di Bari and Dipartimento di Fisica, Università di Bari, I-70126 Bari, Italy*
[4]*University of Bergen, Institute of Physics, N-5007 Bergen, Norway*
[5]*Lawrence Berkeley National Laboratory and University of California, Berkeley, California 94720, USA*
[6]*Ruhr Universität Bochum, Institut für Experimentalphysik 1, D-44780 Bochum, Germany*
[7a]*Institute of Particle Physics, Vancouver, British Columbia V6T 1Z1, Canada*
[7b]*University of British Columbia, Vancouver, British Columbia V6T 1Z1, Canada*
[8a]*Budker Institute of Nuclear Physics SB RAS, Novosibirsk 630090, Russia*
[8b]*Novosibirsk State University, Novosibirsk 630090, Russia*
[8c]*Novosibirsk State Technical University, Novosibirsk 630092, Russia*
[9]*University of California at Irvine, Irvine, California 92697, USA*
[10]*University of California at Riverside, Riverside, California 92521, USA*
[11]*Institute for Particle Physics, University of California at Santa Cruz, Santa Cruz, California 95064, USA*
[12]*California Institute of Technology, Pasadena, California 91125, USA*
[13]*University of Cincinnati, Cincinnati, Ohio 45221, USA*

[14]University of Colorado, Boulder, Colorado 80309, USA
[15]Laboratoire Leprince-Ringuet, Ecole Polytechnique, CNRS/IN2P3, F-91128 Palaiseau, France
[16a]INFN Sezione di Ferrara, I-44122 Ferrara, Italy
[16b]Dipartimento di Fisica e Scienze della Terra, Università di Ferrara, I-44122 Ferrara, Italy
[17]INFN Laboratori Nazionali di Frascati, I-00044 Frascati, Italy
[18]INFN Sezione di Genova, I-16146 Genova, Italy
[19]Humboldt-Universität zu Berlin, Institut für Physik, D-12489 Berlin, Germany
[20]Indian Institute of Technology Guwahati, Guwahati, Assam, 781 039, India
[21]University of Iowa, Iowa City, Iowa 52242, USA
[22]Iowa State University, Ames, Iowa 50011, USA
[23]Johns Hopkins University, Baltimore, Maryland 21218, USA
[24]Laboratoire de l'Accélérateur Linéaire, IN2P3/CNRS et Université Paris-Sud 11, Centre Scientifique d'Orsay, F-91898 Orsay Cedex, France
[25]Lawrence Livermore National Laboratory, Livermore, California 94550, USA
[26]University of Liverpool, Liverpool L69 7ZE, United Kingdom
[27]Queen Mary, University of London, London, E1 4NS, United Kingdom
[28]University of London, Royal Holloway and Bedford New College, Egham, Surrey TW20 0EX, United Kingdom
[29]University of Louisville, Louisville, Kentucky 40292, USA
[30]Johannes Gutenberg-Universität Mainz, Institut für Kernphysik, D-55099 Mainz, Germany
[31]University of Manchester, Manchester M13 9PL, United Kingdom
[32]University of Maryland, College Park, Maryland 20742, USA
[33]Laboratory for Nuclear Science. Massachusetts Institute of Technology, Cambridge, Massachusetts 02139, USA
[34a]Institute of Particle Physics, Montréal, Québec H3A 2T8, Canada
[34b]McGill University, Montréal, Québec H3A 2T8, Canada
[35a]INFN Sezione di Milano, I-20133 Milano, Italy
[35b]Dipartimento di Fisica, Università di Milano, I-20133 Milano, Italy
[36]University of Mississippi, University, Mississippi 38677, USA
[37]Université de Montréal, Physique des Particules, Montréal, Québec H3C 3J7, Canada
[38]INFN Sezione di Napoli and Dipartimento di Scienze Fisiche, Università di Napoli Federico II, I-80126 Napoli, Italy
[39]NIKHEF, National Institute for Nuclear Physics and High Energy Physics, NL-1009 DB Amsterdam, Netherlands
[40]University of Notre Dame, Notre Dame, Indiana 46556, USA
[41]The Ohio State University, Columbus, Ohio 43210, USA
[42a]INFN Sezione di Padova, I-35131 Padova, Italy
[42b]Dipartimento di Fisica, Università di Padova, I-35131 Padova, Italy
[43]Laboratoire de Physique Nucléaire et de Hautes Energies, IN2P3/CNRS, Université Pierre et Marie Curie-Paris6, Université Denis Diderot-Paris7, F-75252 Paris, France
[44a]INFN Sezione di Perugia, I-06123 Perugia, Italy
[44b]Dipartimento di Fisica, Università di Perugia, I-06123 Perugia, Italy
[45a]INFN Sezione di Pisa, I-56127 Pisa, Italy
[45b]Dipartimento di Fisica, Università di Pisa, I-56127 Pisa, Italy
[45c]Scuola Normale Superiore di Pisa, I-56127 Pisa, Italy
[46]Princeton University, Princeton, New Jersey 08544, USA
[47a]INFN Sezione di Roma, I-00185 Roma, Italy
[47b]Dipartimento di Fisica, Università di Roma La Sapienza, I-00185 Roma, Italy
[48]Universität Rostock, D-18051 Rostock, Germany
[49]Rutherford Appleton Laboratory, Chilton, Didcot, Oxon, OX11 0QX, United Kingdom
[50]CEA, Irfu, SPP, Centre de Saclay, F-91191 Gif-sur-Yvette, France
[51]SLAC National Accelerator Laboratory, Stanford, California 94309 USA
[52]University of South Carolina, Columbia, South Carolina 29208, USA
[53]Southern Methodist University, Dallas, Texas 75275, USA
[54]St. Francis Xavier University, Antigonish, Nova Scotia B2G 2W5, Canada
[55]Stanford University, Stanford, California 94305, USA
[56]State University of New York, Albany, New York 12222, USA
[57]Tel Aviv University, School of Physics and Astronomy, Tel Aviv 69978, Israel
[58]University of Tennessee, Knoxville, Tennessee 37996, USA
[59]University of Texas at Austin, Austin, Texas 78712, USA

[60]University of Texas at Dallas, Richardson, Texas 75083, USA
[61a]INFN Sezione di Torino, I-10125 Torino, Italy
[61b]Dipartimento di Fisica, Università di Torino, I-10125 Torino, Italy
[62]INFN Sezione di Trieste and Dipartimento di Fisica, Università di Trieste, I-34127 Trieste, Italy
[63]IFIC, Universitat de Valencia-CSIC, E-46071 Valencia, Spain
[64a]Institute of Particle Physics, Victoria, British Columbia V8W 3P6, Canada
[64b]University of Victoria, Victoria, British Columbia V8W 3P6, Canada
[65]Department of Physics, University of Warwick, Coventry CV4 7AL, United Kingdom
[66]University of Wisconsin, Madison, Wisconsin 53706, USA

(Received 30 October 2018; published 28 December 2018)

We study the processes $e^+e^- \to \pi^+\pi^-\pi^0\pi^0\pi^0\gamma$ and $\pi^+\pi^-\pi^0\pi^0\eta\gamma$ in which an energetic photon is radiated from the initial state. The data are collected with the *BABAR* detector at SLAC. About 14 000 and 4700 events, respectively, are selected from a data sample corresponding to an integrated luminosity of 469 fb^{-1}. The invariant mass of the hadronic final state defines the effective e^+e^- center-of-mass energy. From the mass spectra, the first precise measurement of the $e^+e^- \to \pi^+\pi^-\pi^0\pi^0\pi^0$ cross section and the first measurement ever of the $e^+e^- \to \pi^+\pi^-\pi^0\pi^0\eta$ cross section are performed. The center-of-mass energies range from threshold to 4.35 GeV. The systematic uncertainty is typically between 10% and 13%. The contributions from $\omega\pi^0\pi^0$, $\eta\pi^+\pi^-$, and other intermediate states are presented. We observe the J/ψ and $\psi(2S)$ in most of these final states and measure the corresponding branching fractions, many of them for the first time.

DOI: 10.1103/PhysRevD.98.112015

I. INTRODUCTION

Electron-positron annihilation events with initial-state radiation (ISR) can be used to study processes over a wide range of energies below the nominal e^+e^- center-of-mass (c.m.) energy ($E_{\text{c.m.}}$), as proposed in Ref. [1]. The possibility of exploiting ISR to make precise measurements of low-energy cross sections at high-luminosity ϕ and B factories is discussed in Refs. [2–4], and motivates the studies described in this paper. Such measurements are of particular interest because of an ∼3.5 standard-deviation discrepancy between the measured value of the muon anomalous magnetic moment $(g_\mu - 2)$ and the Standard Model value [5], where the Standard Model calculation requires input from experimental e^+e^- hadronic cross section data in order to account for hadronic vacuum polarization (HVP) terms. The calculation is most sensitive to the low-energy region, where the inclusive hadronic cross section cannot be measured reliably and a sum of exclusive states must be used. Not all accessible states have yet been measured, and new measurements will improve the reliability of the calculation. In addition, studies of ISR events at B factories are interesting in their own right, because they provide information on resonance spectroscopy for masses up to the charmonium region.

Studies of the ISR processes $e^+e^- \to \mu^+\mu^-\gamma$ [6,7] and $e^+e^- \to X_h\gamma$, using data from the *BABAR* experiment at SLAC, have been previously reported. Here X_h represents any of several exclusive hadronic final states. The X_h studied to date include charged hadron pairs $\pi^+\pi^-$ [7], K^+K^- [8], and $p\bar{p}$ [9]; four or six charged mesons [10–12]; charged mesons plus one or two π^0 mesons [11–15]; a K^0_S meson plus charged and neutral mesons [16], and channels with K^0_L mesons [17]. The ISR events are characterized by good reconstruction efficiency and by well-understood kinematics (see for example Ref. [13]), tracking, particle identification, and π^0, K^0_S, and K^0_L reconstruction demonstrated in the above references.

This paper reports analyses of the $\pi^+\pi^-3\pi^0$ and $\pi^+\pi^-2\pi^0\eta$ final states produced in conjunction with a hard photon assumed to result from ISR. While *BABAR* data are available at effective c.m. energies up to 10.58 GeV, the present analysis is restricted to energies below 4.35 GeV because of backgrounds from $\Upsilon(4S)$ decays. As part of the analysis, we search for and observe intermediate states, including the η, ω, ρ, $a_0(980)$, and $a_1(1260)$ resonances.

[*]Deceased.
[†]Present address: Wuhan University, Wuhan 430072, China.
[‡]Present address: Università di Bologna and INFN Sezione di Bologna, I-47921 Rimini, Italy.
[§]Present address: University of Huddersfield, Huddersfield HD1 3DH, United Kingdom.
[¶]Present address: University of South Alabama, Mobile, AL 36688, USA.
[**]Also at Università di Sassari, I-07100 Sassari, Italy.
[††]Also at Gran Sasso Science Institute, I-67100 LAquila, Italy.

A clear J/ψ signal is observed for both the $\pi^+\pi^-3\pi^0$ and $\pi^+\pi^-2\pi^0\eta$ channels, and the corresponding J/ψ branching fractions are measured. The decay $\psi(2S) \to \pi^+\pi^-\pi^0\pi^0\pi^0$ is observed and its branching fraction is measured.

Previous measurements of the $e^+e^- \to \pi^+\pi^-\pi^0\pi^0\pi^0$ cross section were reported by the M3N [18] and MEA [19] experiments, but with very limited precision, leading to a large uncertainty in the corresponding HVP contribution. The *BABAR* experiment previously measured the $e^+e^- \to \eta\pi^+\pi^-$ reaction in the $\eta \to \pi^+\pi^-\pi^0$ [14] and $\eta \to \gamma\gamma$ [20] decay channels. Below, we present the measurement of $e^+e^- \to \eta\pi^+\pi^-$ with $\eta \to \pi^0\pi^0\pi^0$: this process contributes to $e^+e^- \to \pi^+\pi^-\pi^0\pi^0\pi^0$. There are no previous results for $e^+e^- \to \pi^+\pi^-\pi^0\pi^0\eta$.

II. THE *BABAR* DETECTOR AND DATA SET

The data used in this analysis were collected with the *BABAR* detector at the PEP-II2 asymmetric energy e^+e^- storage ring. The total integrated luminosity used is 468.6 fb^{-1} [21], which includes data collected at the $\Upsilon(4S)$ resonance (424.7 fb^{-1}) and at a c.m. energy 40 MeV below this resonance (43.9 fb^{-1}).

The *BABAR* detector is described in detail elsewhere [22]. Charged particles are reconstructed using the *BABAR* tracking system, which is comprised of the silicon vertex tracker (SVT) and the drift chamber (DCH), both located inside the 1.5 T solenoid. Separation of pions and kaons is accomplished by means of the detector of internally reflected Cherenkov light and energy-loss measurements in the SVT and DCH. Photons and K^0_L mesons are detected in the electromagnetic calorimeter (EMC). Muon identification is provided by the instrumented flux return.

To evaluate the detector acceptance and efficiency, we have developed a special package of Monte Carlo (MC) simulation programs for radiative processes based on the approach of Czyż and Kühn [23]. Multiple collinear soft-photon emission from the initial e^+e^- state is implemented with the structure function technique [24,25], while additional photon radiation from final-state particles is simulated using the PHOTOS package [26]. The precision of the radiative simulation is such that it contributes less than 1% to the uncertainty in the measured hadronic cross sections.

We simulate $e^+e^- \to \pi^+\pi^-\pi^0\pi^0\pi^0\gamma$ events assuming production through the $\omega(782)\pi^0\pi^0$ and $\eta\rho(770)$ intermediate channels, with decay of the ω to three pions and decay of the η to all its measured decay modes [27]. The two neutral pions in the $\omega\pi^0\pi^0$ system are in an S-wave state and are described by a combination of phase space and $f_0(980) \to \pi^0\pi^0$ based on our study of the $\omega\pi^+\pi^-$ state [14]. The simulation of $e^+e^- \to \pi^+\pi^-\pi^0\pi^0\eta\gamma$ events is similarly based on two production channels: a phase space model, and a model with an $\omega\pi^0\eta$ intermediate state with a $\pi^0\eta$ S-wave system.

A sample of 100–200 k simulated events is generated for each signal reaction and processed through the detector response simulation based on the GEANT4 package [28]. These events are reconstructed using the same software chain as the data. Variations in detector and background conditions are taken into account.

For the purpose of background estimation, large samples of events from the main relevant ISR processes ($2\pi\gamma$, $3\pi\gamma$, $4\pi\gamma$, $5\pi\gamma$, $2K\pi\gamma$, and $\pi^+\pi^-\pi^0\pi^0\gamma$) are simulated. To evaluate the background from the relevant non-ISR processes, namely $e^+e^- \to q\bar{q}$ ($q = u, d, s$) and $e^+e^- \to \tau^+\tau^-$, simulated samples with integrated luminosities about twice that of the data are generated using the JETSET [29] and KORALB [30] programs, respectively. The cross sections for the above processes are known with an accuracy slightly better than 10%, which is sufficient for the present purposes.

III. EVENT SELECTION AND KINEMATIC FIT

A relatively clean sample of $\pi^+\pi^-3\pi^0\gamma$ and $\pi^+\pi^-2\pi^0\eta\gamma$ events is selected by requiring that there be two tracks reconstructed in the DCH, SVT, or both, and seven or more photons, with an energy above 0.02 GeV, in the EMC. We assume the photon with the highest energy to be the ISR photon, and we require its c.m. energy to be larger than 3 GeV.

We allow either exactly two or exactly three tracks in an event, but only two that extrapolate to within 0.25 cm of the beam axis and 3.0 cm of the nominal collision point along that axis. The reason a third track is allowed is to capture a relatively small fraction of signal events that contain a background track. The two tracks that satisfy the extrapolation criteria are fit to a vertex, which is used as the point of origin in the calculation of the photon directions.

We subject each candidate event to a set of constrained kinematic fits and use the fit results, along with charged-particle identification, to select the final states of interest and evaluate backgrounds from other processes. The kinematic fits make use of the four-momenta and covariance matrices of the initial e^+, e^-, and the set of selected tracks and photons. The fitted three-momenta of each track and photon are then used in further kinematical calculations.

Excluding the photon with the highest c.m. energy, which is assumed to arise from ISR, six other photons are combined into three pairs. For each set of six photons, there are 15 independent combinations of photon pairs. We retain those combinations in which the diphoton mass of at least two pairs lies within 35 MeV/c^2 of the π^0 mass m_{π^0}. The selected combinations are subjected to a fit in which the diphoton masses of the two pairs with $|m(\gamma\gamma) - m_{\pi^0}| < 35$ MeV/c^2 are constrained to m_{π^0}. In combination with the constraints due to four-momentum conservation, there are thus six constraints (6C) in the fit. The photons in the remaining ("third") pair are treated as being independent. If all three photon pairs in the combination satisfy

$|m(\gamma\gamma) - m_{\pi^0}| < 35$ MeV/c^2, we test all possible combinations, allowing each of the three diphoton pairs in turn to be the third pair, i.e., the pair without the m_{π^0} constraint.

The above procedure allows us not only to search for events with $\pi^0 \to \gamma\gamma$ in the third photon pair, but also for events with $\eta \to \gamma\gamma$.

The 6C fit is performed under the signal hypothesis $e^+e^- \to \pi^+\pi^-\pi^0\pi^0\gamma\gamma\gamma_{\rm ISR}$. The combination with the smallest χ^2 is retained, along with the obtained $\chi^2{}_{2\pi2\pi^0\gamma\gamma}$ value and the fitted three-momenta of each track and photon. Each selected event is also subjected to a 6C fit under the $e^+e^- \to \pi^+\pi^-\pi^0\pi^0\gamma_{\rm ISR}$ background hypothesis, and the $\chi^2_{2\pi2\pi^0}$ value is retained. The $\pi^+\pi^-\pi^0\pi^0$ process has a larger cross section than the $\pi^+\pi^-3\pi^0$ signal process and can contribute to the background when two background photons are present. Most events contain additional soft photons due to machine background or interactions in the detector material.

IV. THE $\pi^+\pi^-3\pi^0$ FINAL STATE

A. Additional selection criteria

The results of the 6C fit to events with two tracks and at least seven photon candidates are used to perform the final selection of the five-pion sample. We require the tracks to lie within the fiducial region of the DCH (0.45–2.40 rad) and to be inconsistent with being a kaon or muon. The photon candidates are required to lie within the fiducial region of the EMC (0.35–2.40 rad) and to have an energy larger than 0.035 GeV. A requirement that there be no charged tracks within 1 rad of the ISR photon reduces the $\tau^+\tau^-$ background to a negligible level. A requirement that any extra photons in an event each have an energy below 0.7 GeV slightly reduces the multiphoton background.

Figure 1(a) shows the invariant mass $m(\gamma\gamma)$ of the third photon pair vs $\chi^2_{2\pi2\pi^0\gamma\gamma}$. Clear π^0 and η peaks are visible at small χ^2 values. We require $\chi^2_{2\pi2\pi^0\gamma\gamma} < 60$ for the signal hypothesis and $\chi^2_{2\pi2\pi^0} > 30$ for the $2\pi2\pi^0$ background hypothesis. This requirement reduces the contamination due to $2\pi2\pi^0$ events from 30% to about 1%–2% while reducing the signal efficiency by only 5%.

Figure 1(b) shows the $m(\gamma\gamma)$ distribution after the above requirements have been applied. The dip in this distribution at the π^0 mass value is a consequence of the kinematic fit constraint of the best two photon pairs to the π^0 mass. Also, because of this constraint, the third photon pair is sometimes formed from photon candidates that are less well measured.

Figure 2 shows the $m(\gamma\gamma)$ distribution vs the invariant mass $m(2\pi2\pi^0\gamma\gamma)$ for events, Fig. 2(a), in the signal region $\chi^2_{2\pi2\pi^0\gamma\gamma} < 60$ and, Fig. 2(b), in a control region defined by $60 < \chi^2_{2\pi2\pi^0\gamma\gamma} < 120$. Events from the $e^+e^- \to \pi^+\pi^-\pi^0\pi^0\pi^0$ and $\pi^+\pi^-2\pi^0\eta$ processes are clearly seen in the signal region, as well as J/ψ decays to these final states. In the control region no significant structures are seen and we use these events to evaluate background.

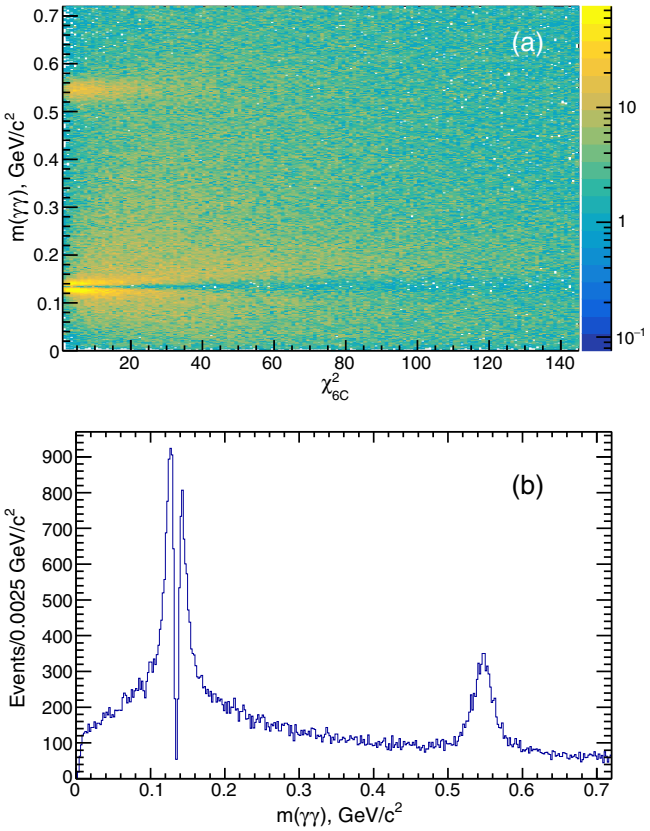

FIG. 1. (a) The invariant mass $m(\gamma\gamma)$ of the third photon pair vs $\chi^2_{2\pi2\pi^0\gamma\gamma}$. (b) The $m(\gamma\gamma)$ distribution for $\chi^2_{2\pi2\pi^0\gamma\gamma} < 60$ and with additional selection criteria applied as described in the text.

Our strategy to extract the signals for the $e^+e^- \to \pi^+\pi^-\pi^0\pi^0\pi^0$ and $\pi^+\pi^-\pi^0\pi^0\eta$ processes is to perform a fit for the π^0 and η yields in intervals of 0.05 GeV/c^2 in the distribution of the $\pi^+\pi^-2\pi^0\gamma\gamma$ invariant mass $m(\pi^+\pi^-2\pi^0\gamma\gamma)$.

B. Detection efficiency

As mentioned in Sec. II, the model used in the MC simulation assumes that the five-pion final state results predominantly from $\omega\pi^0\pi^0$ and $\eta\pi^+\pi^-$ production, with ω decays to three pions and η decays to all modes. As shown below, these two final states dominate the observed cross section.

The selection procedure applied to the data is also applied to the MC-simulated events. Figures 3(a) and 4(a) show the $m(\gamma\gamma)$ distribution and Figs. 3(b) and 4(b) show the distribution of $m(\gamma\gamma)$ vs $m(2\pi2\pi^0\gamma\gamma)$ for the simulated $\eta\pi^+\pi^-$ and $\omega\pi^0\pi^0$ events, respectively. The π^0 peak is not Gaussian in either reaction and is broader for $\eta\pi^+\pi^-$ events than for $\omega\pi^0\pi^0$ events because the photon

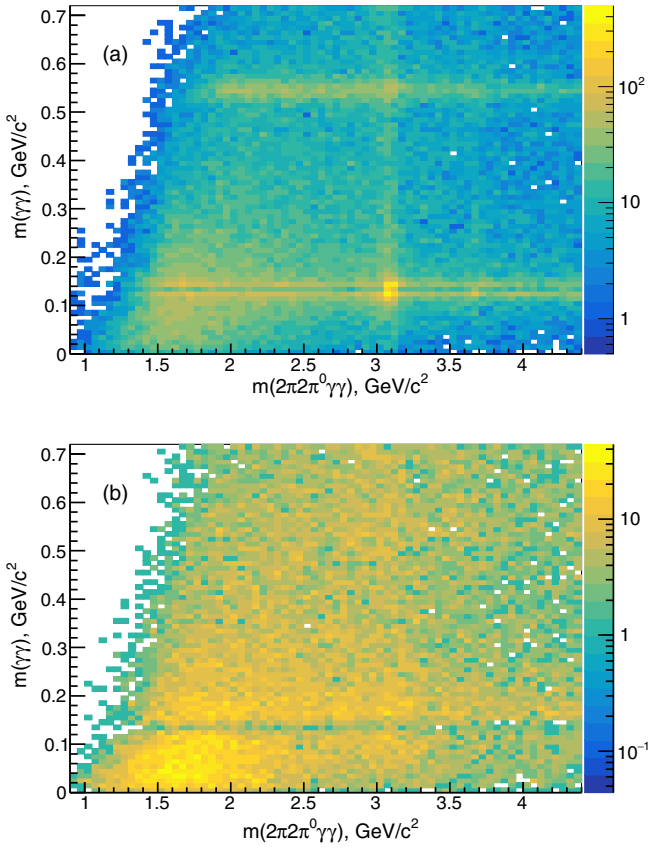

FIG. 2. (a) The third-photon-pair invariant mass $m(\gamma\gamma)$ vs $m(2\pi2\pi^0\gamma\gamma)$ for (a) $\chi^2_{2\pi2\pi^0\gamma\gamma} < 60$ and (b) $60 < \chi^2_{2\pi2\pi^0\gamma\gamma} < 120$.

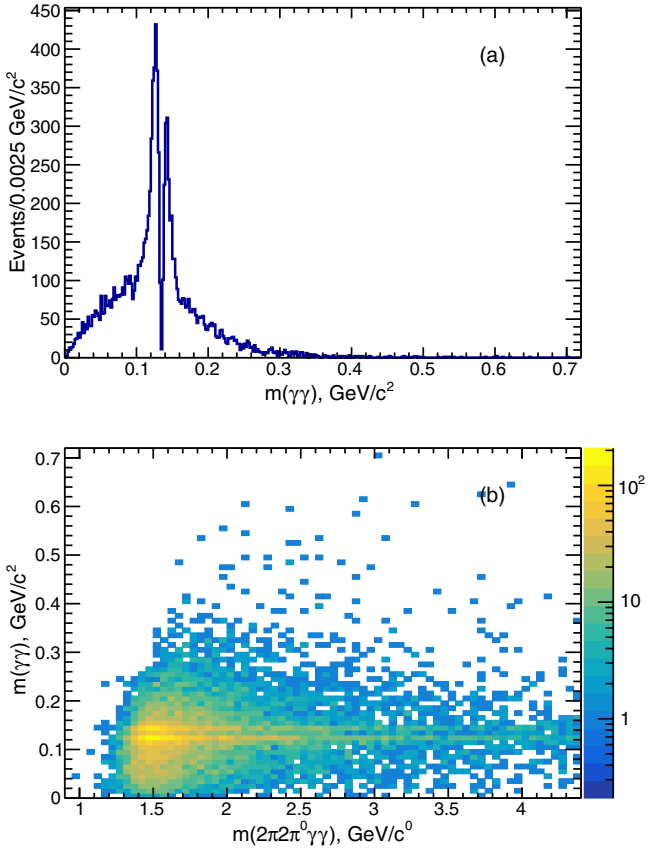

FIG. 3. The MC-simulated distribution for $e^+e^- \to \eta\pi^+\pi^-$ events of (a) the third-photon-pair invariant mass $m(\gamma\gamma)$, and (b) $m(\gamma\gamma)$ vs $m(\pi^+\pi^-2\pi^0\gamma\gamma)$.

energies are lower. Background photons are included in the simulation. Thus these distributions include simulation of the combinatoric background that arises when background photons are combined with photons from the signal reactions.

The combinatoric background is subtracted using the data from the χ^2 control region. The method is illustrated using simulation in Fig. 5, which shows the $m(\gamma\gamma)$ distribution with a bin width of 0.02 GeV/c^2. The dashed histograms show the simulated combinatoric background. The solid histograms show the simulated results from the signal region after subtraction of the simulated combinatoric background. The sum of three Gaussian functions with a common mean is used to describe the π^0 signal shape. The fitted fit function is shown by the smooth curve in Fig. 5. We perform a fit of the π^0 signal in every 0.05 GeV/c^2 interval in the $m(2\pi2\pi^0\gamma\gamma)$ invariant mass for the two different simulated channels.

Alternatively, for the $\eta\pi^+\pi^-$ events, we determine the number of events vs the $m(2\pi2\pi^0\gamma\gamma)$ invariant mass by fitting the η signal from the $\eta \to \pi^0\pi^0\pi^0$ decay: the simulated background-subtracted distribution is shown in Fig. 6(a). The fit function is again the sum of three Gaussian functions with a common mean.

Similarly, as an alternative for the $\omega\pi^0\pi^0$ events, the ω mass peak can be used. The ω mass peak in simulation is shown in Fig. 6(b), with three entries per event. We obtain the number of events by fitting $m(\pi^+\pi^-\pi^0)$ in 0.05 GeV/c^2 intervals of the $m(\pi^+\pi^-2\pi^0\gamma\gamma)$ invariant mass. A Breit-Wigner (BW) function convoluted with a Gaussian distribution to account for the detector resolution is used to describe the ω signal. A second-order polynomial is used to describe the background.

The mass-dependent detection efficiency is obtained by dividing the number of fitted MC events in each 0.05 GeV/c^2 mass interval by the number generated in the same interval. Although the signal simulation accounts for all η decay modes, the efficiency calculation considers the signal $\eta \to \pi^0\pi^0\pi^0$ decay mode only. This efficiency estimate takes into account the geometrical acceptance of the detector for the final-state photons and the charged pions, the inefficiency of the detector subsystems, and the event loss due to additional soft-photon emission from the initial and final states. Corrections that account for data versus MC differences are discussed below.

The mass-dependent efficiencies from the π^0 fit are shown in Fig. 7 by points for the $\eta\pi^+\pi^-$ and by squares for the $\omega\pi^0\pi^0$ intermediate states, respectively.

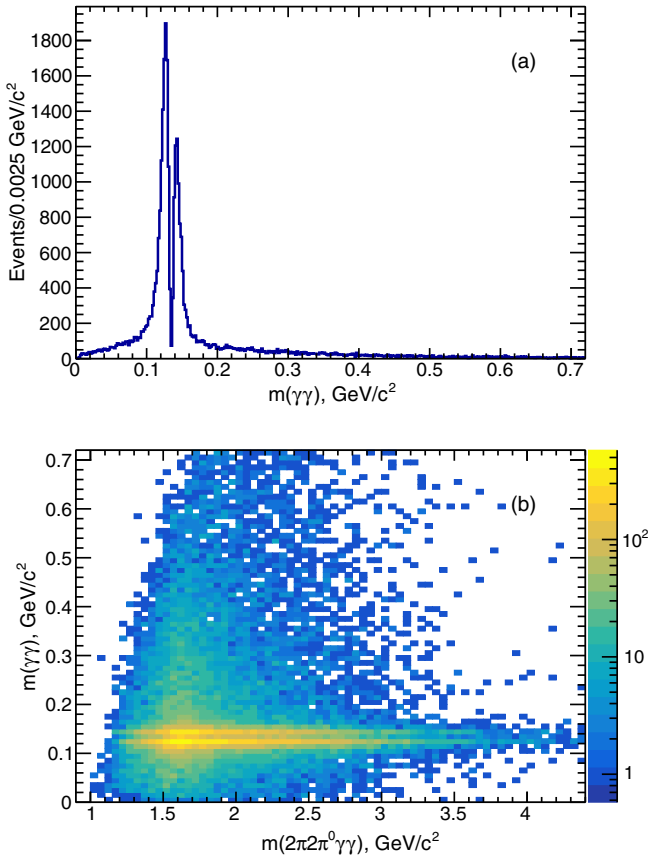

FIG. 4. The MC-simulated distribution for $e^+e^- \to \omega\pi^0\pi^0$ events of (a) the third-photon-pair invariant mass $m(\gamma\gamma)$, and (b) $m(\gamma\gamma)$ vs $m(\pi^+\pi^-2\pi^0\gamma\gamma)$.

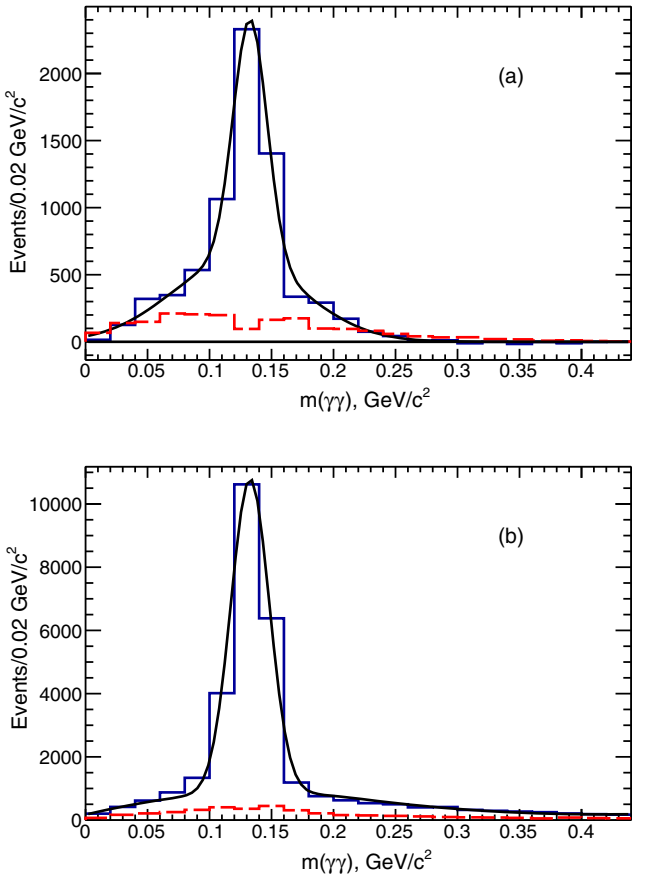

FIG. 5. The background-subtracted MC-simulated $m(\gamma\gamma)$ distribution for (a) $e^+e^- \to \eta\pi^+\pi^-$ and (b) $e^+e^- \to \omega\pi^0\pi^0$ events. The dashed histogram shows the simulated distribution from the χ^2 control region used for subtraction. The fit function is described in the text.

The efficiencies determined from the η and ω fits are shown in Fig. 7 by the triangles and upside-down triangles, respectively. These results are very similar to those obtained from the π^0 fits.

From Fig. 7 it is seen that the reconstruction efficiency is about 4%, roughly independent of mass. By comparing the results of the four different methods used to evaluate the efficiency, we conclude that the overall acceptance does not change by more than 5% because of variations of the functions used to extract the number of events or the use of different models. This value is taken as an estimate of the systematic uncertainty in the acceptance associated with the simulation model used and with the fit procedure. We average the four efficiencies in each 0.05 GeV/c^2 mass interval and fit the result with a third-order polynomial function shown in Fig. 7. The result of this fit is used for the cross section calculation.

C. Number of $\pi^+\pi^-3\pi^0$ events

The solid histogram in Fig. 8(a) shows the $m(\gamma\gamma)$ data of Fig. 1(b) binned in mass intervals of 0.02 GeV/c^2. The dashed histogram shows the distribution of data from the χ^2 control region. The dotted histogram is the estimated remaining background from the $e^+e^- \to \pi^+\pi^-\pi^0\pi^0$ process. No evidence for a peaking background is seen in either of the two background distributions. We subtract the background evaluated using the χ^2 control region. The resulting $m(\gamma\gamma)$ distribution is shown in Fig. 8(b).

We fit the data of Fig. 8(b) with a combination of a signal function taken from simulation, and a background function taken to be a third-order polynomial. The fit is performed in the $m(\gamma\gamma)$ mass range from 0.0 to 0.5 GeV/c^2. The result of the fit is shown by the solid and dashed curves in Fig. 8(b). In total $14\,390 \pm 182$ events are obtained. Note that this number includes a relatively small peaking-background component, due to $q\bar{q}$ events, which is discussed in Sec. IV D. The same fit is applied to the corresponding $m(\gamma\gamma)$ distribution in each 0.05 GeV/c^2 interval in the $\pi^+\pi^-2\pi^0\gamma\gamma$ invariant mass. The resulting number of $\pi^+\pi^-3\pi^0$ event candidates as a function of $m(\pi^+\pi^-3\pi^0)$, including the peaking $q\bar{q}$ background, is shown by the data points in Fig. 9.

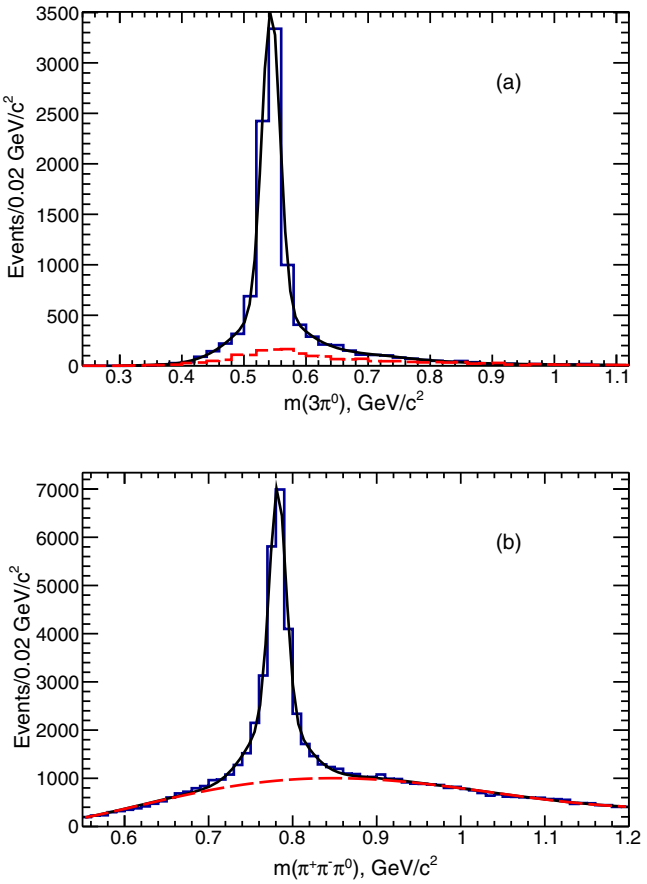

FIG. 6. (a) The background-subtracted MC-simulated $3\pi^0$ invariant mass for the $e^+e^- \to \eta\pi^+\pi^-$ events. The dashed distribution is from the simulated χ^2 control region used for background subtraction. (b) The $\pi^+\pi^-\pi^0$ invariant mass for the MC-simulated $e^+e^- \to \omega\pi^0\pi^0$ events (three entries per event). The solid curve shows the fit function used to obtain the number of signal events. The dashed curve shows the fit function for the combinatorial background.

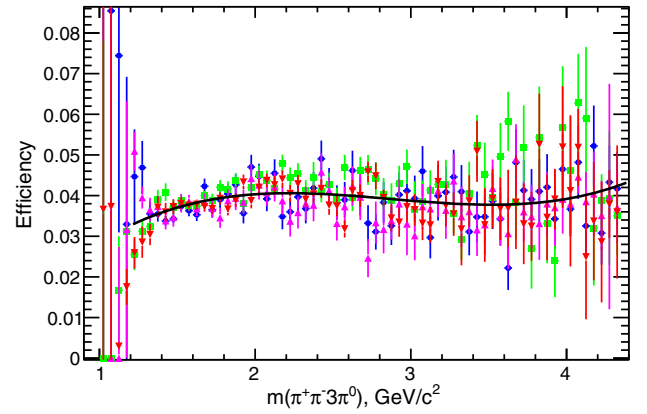

FIG. 7. The energy-dependent reconstruction efficiency for $e^+e^- \to \pi^+\pi^-\pi^0\pi^0\pi^0$ events determined using four different methods; see text. The curve shows the results of a fit to the average values, which is used in the cross section calculation.

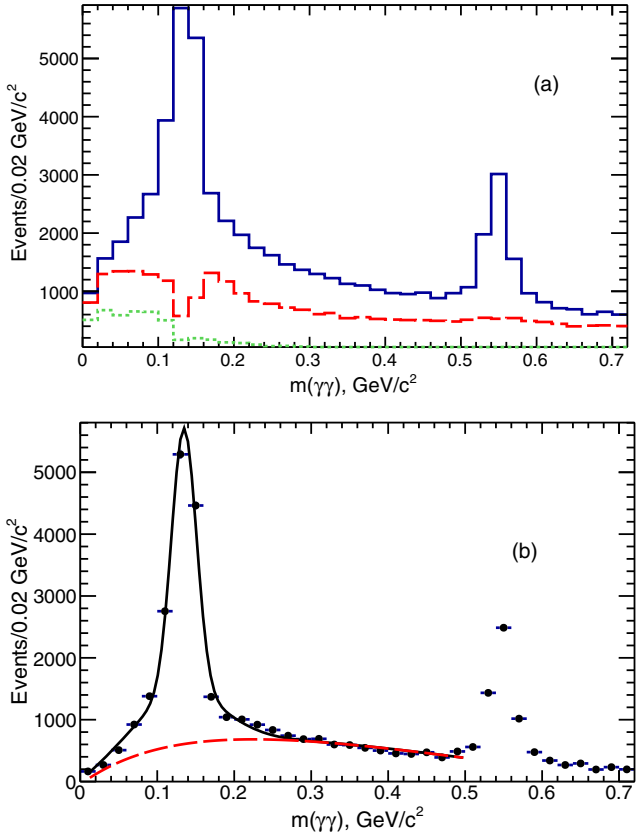

FIG. 8. (a) The third-photon-pair invariant mass $m(\gamma\gamma)$ for data in the signal (solid) and χ^2 control (dashed) regions. The dotted histogram shows the estimated background from $e^+e^- \to \pi^+\pi^-\pi^0\pi^0$. (b) The $m(\gamma\gamma)$ invariant mass for data after background subtraction. The curves are the fit results as described in the text.

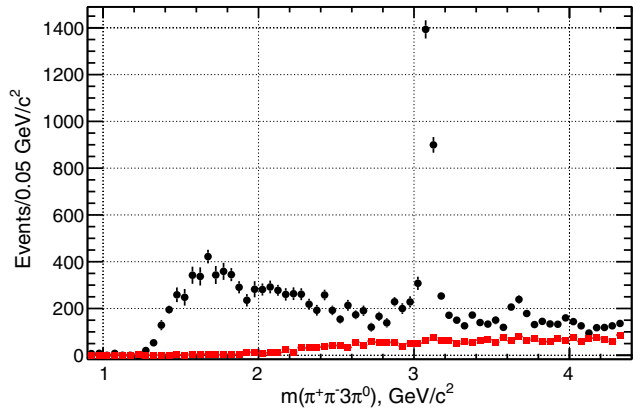

FIG. 9. The invariant mass distribution of $\pi^+\pi^-3\pi^0$ events obtained from the fit to the π^0 mass peak. The contribution from non-ISR *uds* background is shown by squares.

D. Peaking background

The major background producing a π^0 peak following application of the selection criteria of Sec. IV A is from

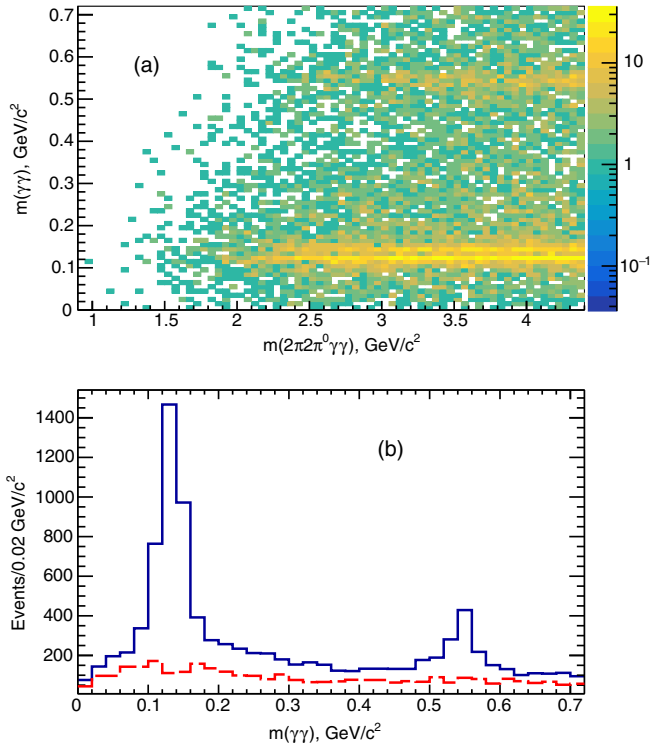

FIG. 10. (a) The third-photon-pair invariant mass vs $m(\pi^+\pi^-\pi^0\pi^0\gamma\gamma)$ for the *uds* simulation. (b) The projection plot for (a) the signal region $\chi^2_{2\pi2\pi^0\gamma\gamma} < 60$ (solid histogram), and the control region $60 < \chi^2_{2\pi2\pi^0\gamma\gamma} < 120$ (dashed histogram).

non-ISR $q\bar{q}$ events, the most important channel being $e^+e^- \to \pi^+\pi^-\pi^0\pi^0\pi^0\pi^0$ in which one of the neutral pions decays asymmetrically, yielding a high-energy photon that mimics an ISR photon. Figure 10(a) shows the third-photon-pair invariant mass vs $m(\pi^+\pi^-\pi^0\pi^0\gamma\gamma)$ for the non-ISR light quark $q\bar{q}$ (uds) simulation: clear signals from π^0 and η are seen. Figure 10(b) shows the projection plots for $\chi^2_{2\pi2\pi^0\gamma\gamma} < 60$ and $60 < \chi^2_{2\pi2\pi^0\gamma\gamma} < 120$.

To normalize the *uds* simulation, we calculate the diphoton invariant mass distribution of the ISR candidate with all the remaining photons in the event. A π^0 peak is observed, with approximately the same number of events in data and simulation, leading to a normalization factor of 1.0 ± 0.1. The resulting *uds* background is shown by the squares in Fig. 9: The *uds* background is negligible below 2 GeV/c^2, but accounts for more than half the total background for around 4 GeV/c^2 and above.

E. Cross section for $e^+e^- \to \pi^+\pi^-\pi^0\pi^0\pi^0$

The $e^+e^- \to \pi^+\pi^-\pi^0\pi^0\pi^0$ Born cross section is determined from

$$\sigma(2\pi3\pi^0)(E_{\rm c.m.}) = \frac{dN_{5\pi\gamma}(E_{\rm c.m.})}{d\mathcal{L}(E_{\rm c.m.})\epsilon^{\rm corr}_{5\pi}\epsilon^{\rm MC}_{5\pi}(E_{\rm c.m.})(1+\delta_R)}, \quad (1)$$

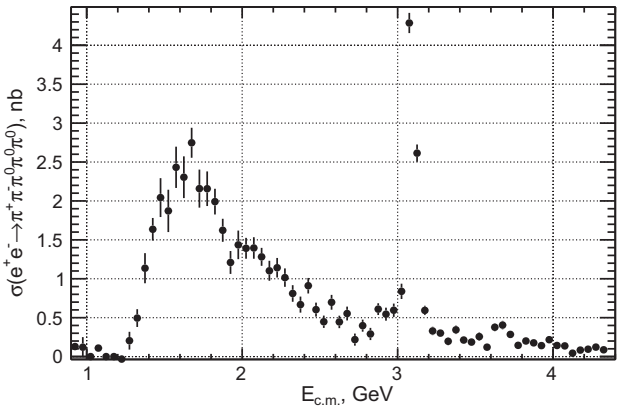

FIG. 11. The measured $e^+e^- \to \pi^+\pi^-\pi^0\pi^0\pi^0$ cross section. The uncertainties are statistical only.

where $E_{\rm c.m.}$ is the invariant mass of the five-pion system; $dN_{5\pi\gamma}$ is the background-subtracted number of selected five-pion events in the interval $dE_{\rm c.m.}$, and $\epsilon^{\rm MC}_{5\pi}(E_{\rm c.m.})$ is the corresponding detection efficiency from simulation. The factor $\epsilon^{\rm corr}_{5\pi}$ accounts for the difference between data and simulation in the tracking ($1.0 \pm 1.0\%$/per track) [10] and π^0 ($3.0 \pm 1.0\%$ per pion) [15] reconstruction efficiencies. The ISR differential luminosity $d\mathcal{L}$ is calculated using the total integrated *BABAR* luminosity of 469 fb^{-1} [13]. The initial- and final-state soft-photon emission is accounted for by the radiative correction factor $(1+\delta_R)$, which is close to unity for our selection criteria. The cross section results contain the effect of vacuum polarization because this effect is not accounted for in the luminosity calculation.

Our results for the $e^+e^- \to \pi^+\pi^-\pi^0\pi^0\pi^0$ cross section are shown in Fig. 11. The cross section exhibits a structure around 1.7 GeV with a peak value of about 2.5 nb, followed by a monotonic decrease toward higher energies. Because we present our data in bins of width 0.050 GeV/c^2, compatible with the experimental resolution, we do not apply an unfolding procedure to the data. Numerical values for the cross section are presented in Table I. The J/ψ region is discussed later.

F. Summary of the systematic studies

The systematic uncertainties presented in the previous sections are summarized in Table II, along with the corrections that are applied to the measurements.

The three corrections applied to the cross sections sum up to 12.5%. The systematic uncertainties vary from 10% for $E_{\rm c.m.} < 2.5$ GeV to 50% for $E_{\rm c.m.} > 3.5$ GeV. The largest systematic uncertainty arises from the fitting and background-subtraction procedures. It is estimated by varying the background levels and the parameters of the functions used.

G. Overview of the intermediate structures

The $e^+e^- \to \pi^+\pi^-\pi^0\pi^0\pi^0$ process has a rich internal substructure. To study this substructure, we restrict events

TABLE I. Summary of the $e^+e^- \to \pi^+\pi^-\pi^0\pi^0\pi^0$ cross section measurement. The uncertainties are statistical only.

$E_{\rm c.m.}$ (GeV)	σ (nb)	$E_{\rm c.m.}$ (GeV)	σ (nb)	$E_{\rm c.m.}$ (GeV)	σ (nb)	$E_{\rm c.m.}$ (GeV)	σ (nb)	$E_{\rm c.m.}$ (GeV)	σ (nb)
1.125	0.00 ± 0.02	1.775	2.20 ± 0.23	2.425	0.92 ± 0.10	3.075	4.36 ± 0.13	3.725	0.29 ± 0.05
1.175	0.00 ± 0.03	1.825	2.03 ± 0.17	2.475	0.61 ± 0.09	3.125	2.66 ± 0.11	3.775	0.15 ± 0.04
1.225	-0.03 ± 0.05	1.875	1.65 ± 0.15	2.525	0.45 ± 0.08	3.175	0.60 ± 0.06	3.825	0.20 ± 0.04
1.275	0.21 ± 0.12	1.925	1.23 ± 0.15	2.575	0.71 ± 0.10	3.225	0.33 ± 0.05	3.875	0.18 ± 0.04
1.325	0.51 ± 0.12	1.975	1.46 ± 0.19	2.625	0.45 ± 0.08	3.275	0.31 ± 0.05	3.925	0.14 ± 0.04
1.375	1.17 ± 0.20	2.025	1.41 ± 0.14	2.675	0.56 ± 0.09	3.325	0.20 ± 0.05	3.975	0.22 ± 0.04
1.425	1.68 ± 0.15	2.075	1.42 ± 0.14	2.725	0.22 ± 0.08	3.375	0.35 ± 0.05	4.025	0.14 ± 0.04
1.475	2.10 ± 0.26	2.125	1.30 ± 0.12	2.775	0.40 ± 0.08	3.425	0.22 ± 0.05	4.075	0.14 ± 0.03
1.525	1.92 ± 0.28	2.175	1.12 ± 0.13	2.825	0.29 ± 0.08	3.475	0.19 ± 0.05	4.125	0.04 ± 0.03
1.575	2.49 ± 0.27	2.225	1.16 ± 0.13	2.875	0.62 ± 0.08	3.525	0.26 ± 0.05	4.175	0.08 ± 0.03
1.625	2.36 ± 0.27	2.275	1.03 ± 0.12	2.925	0.55 ± 0.08	3.575	0.12 ± 0.05	4.225	0.09 ± 0.03
1.675	2.81 ± 0.20	2.325	0.82 ± 0.11	2.975	0.60 ± 0.09	3.625	0.38 ± 0.05	4.275	0.12 ± 0.03
1.725	2.20 ± 0.25	2.375	0.68 ± 0.10	3.025	0.85 ± 0.10	3.675	0.41 ± 0.06	4.325	0.09 ± 0.03

TABLE II. Summary of the systematic uncertainties in the $e^+e^- \to \pi^+\pi^-\pi^0\pi^0\pi^0$ cross section measurement.

Source	Correction	Uncertainty
Luminosity	...	1%
MC-data difference ISR		
Photon efficiency	+1.5%	1%
χ^2 cut uncertainty	...	3%
Fit and background subtraction	...	7%
$E_{\rm c.m.} > 2.5$ GeV	...	20%
$E_{\rm c.m.} > 3.5$ GeV	...	50%
MC-data difference in track losses	+2%	2%
MC-data difference in π^0 losses	+9%	3%
Radiative corrections accuracy	...	1%
Acceptance from MC (Model dependent)	...	5%
Total (assuming no correlations)	+12.5%	10%
$E_{\rm c.m.} > 2.5$ GeV		21%
$E_{\rm c.m.} > 3.5$ GeV		50%

to $m(\gamma\gamma) < 0.35$ GeV/c^2, eliminating the region populated by $e^+e^- \to \pi^+\pi^-\pi^0\pi^0\eta$. We then assume that the $m(\pi^+\pi^-2\pi^0\gamma\gamma)$ invariant mass can be taken to represent $m(\pi^+\pi^-3\pi^0)$.

Figure 12(a) shows the distribution of the $\pi^0\pi^0\pi^0$ invariant mass. The distribution is seen to exhibit a prominent η peak, which is due to the $e^+e^- \to \eta\pi^+\pi^-$ reaction. Figure 12(b) presents a scatter plot of the $\pi^+\pi^-$ vs the $3\pi^0$ invariant mass. From this plot, the $\rho(770)\eta$ intermediate state is seen to dominate. Figure 12(c) presents a scatter plot of the $3\pi^0$ invariant mass versus $m(\pi^+\pi^-\pi^0\pi^0\gamma\gamma)$.

The distribution of the $\pi^+\pi^-\pi^0$ invariant mass (three entries per event) is shown in Fig. 13(a). A prominent ω peak from $e^+e^- \to \omega\pi^0\pi^0$ is seen. Some indications of ϕ and J/ψ peaks are also present. The scatter plot in Fig. 13 (b) shows the $\pi^0\pi^0$ vs the $\pi^+\pi^-\pi^0$ invariant mass. A scatter plot of the $\pi^+\pi^-\pi^0$ vs the $\pi^+\pi^-\pi^0\pi^0\gamma\gamma$ mass is shown in Fig. 13(c). A clear signal for a J/ψ peak is seen.

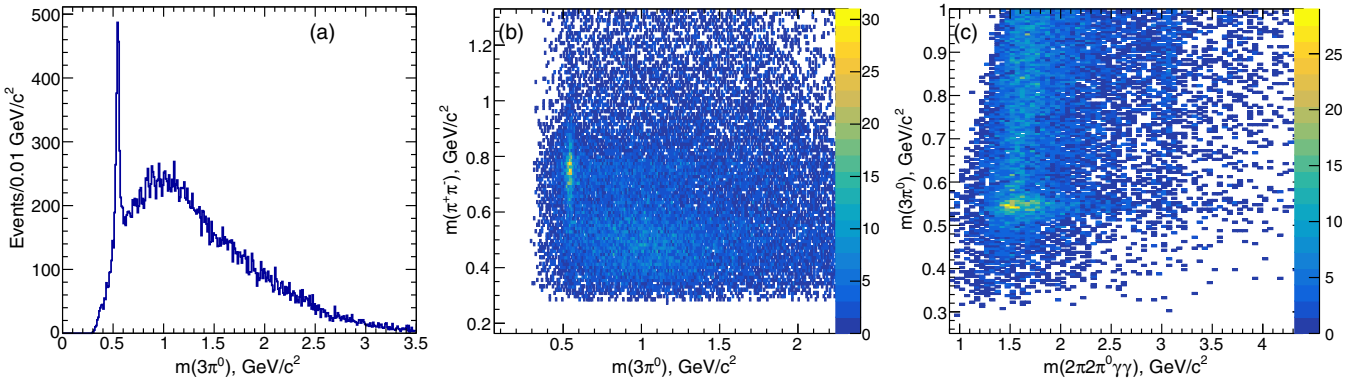

FIG. 12. (a) The $\pi^0\pi^0\pi^0$ invariant mass. (b) The $\pi^+\pi^-$ vs the $\pi^0\pi^0\pi^0$ invariant mass. (c) The $\pi^0\pi^0\pi^0$ invariant mass vs the five-pion invariant mass.

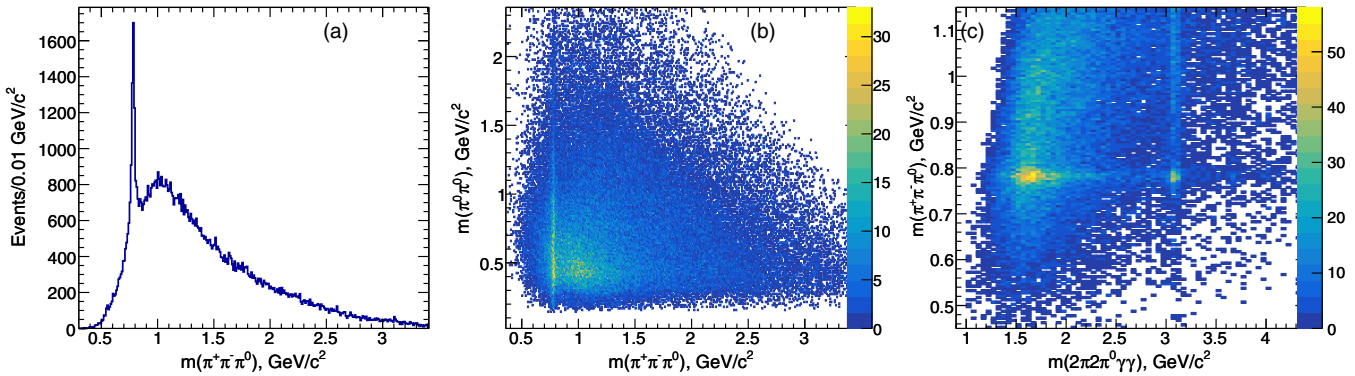

FIG. 13. (a) The $\pi^+\pi^-\pi^0$ invariant mass (three combinations per event). (b) The $\pi^0\pi^0$ vs the $\pi^+\pi^-\pi^0$ invariant mass. (c) The $\pi^+\pi^-\pi^0$ invariant mass vs the five-pion invariant mass.

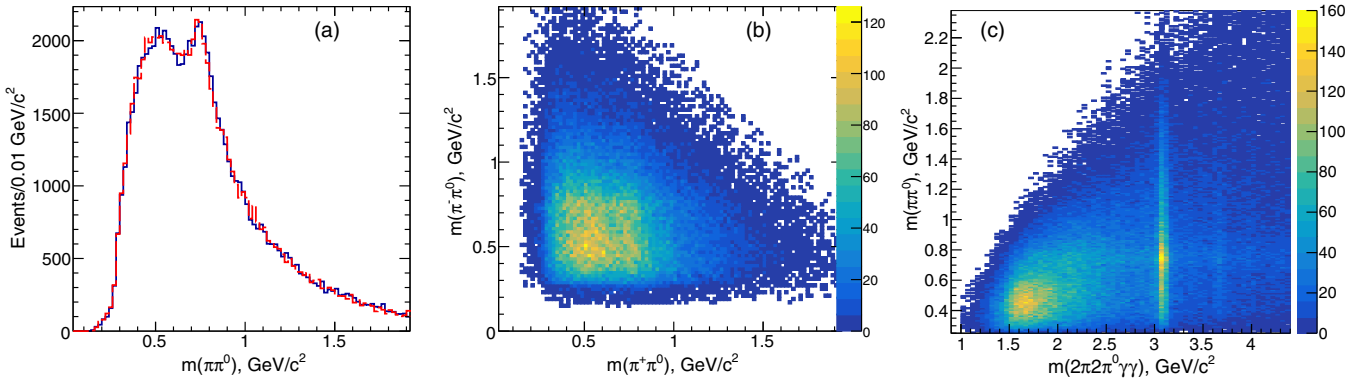

FIG. 14. (a) The $\pi^+\pi^0$ (solid) and $\pi^-\pi^0$ (dashed) invariant masses (three combinations per event). (b) The $\pi^-\pi^0$ vs the $\pi^+\pi^0$ invariant mass. (c) The $\pi^\pm\pi^0$ invariant mass vs the five-pion invariant mass.

Figure 14(a) shows the $\pi^+\pi^0$ (dotted) and $\pi^-\pi^0$ (solid) invariant masses (three entries per event). A prominent $\rho(770)$ peak, corresponding to $e^+e^- \to 3\pi\rho$, is visible. The scatter plot in Fig. 14(b) shows the $\pi^-\pi^0$ vs the $\pi^+\pi^0$ invariant mass. An indication of the $\rho^+\rho^-\pi^0$ intermediate state is visible. Figure 14(c) shows the $\pi\pi^0$ invariant mass vs the five-pion invariant mass: a clear signal for the J/ψ and an indication of the $\psi(2S)$ are seen.

H. The $\eta\pi^+\pi^-$ intermediate state

To determine the contribution of the $\eta\pi^+\pi^-$ intermediate state, we fit the events of Fig. 12(a) using a triple-Gaussian function to describe the signal peak, as in Fig. 6(a), and a polynomial to describe the background. The result of the fit is shown in Fig. 15(a). We obtain 2102 ± 112 $\eta\pi^+\pi^-$ events. The number of $\eta\pi^+\pi^-$ events as a function of the five-pion invariant mass is determined by performing an analogous fit of events in Fig. 12(c) in each 0.05 GeV/c^2 interval of $m(\pi^+\pi^-3\pi^0)$. The resulting distribution is shown in Fig. 16.

The $\pi^+\pi^-$ invariant mass distribution for events within ± 0.7 GeV/c^2 of the η peak in Fig. 15(a) is shown in Fig. 15(b). A clear signal from $\rho(770)$ is observed, supporting the statement that the reaction is dominated by the $\rho(770)\eta$ intermediate state. The distribution of events from η-peak sidebands is shown by the dashed histogram.

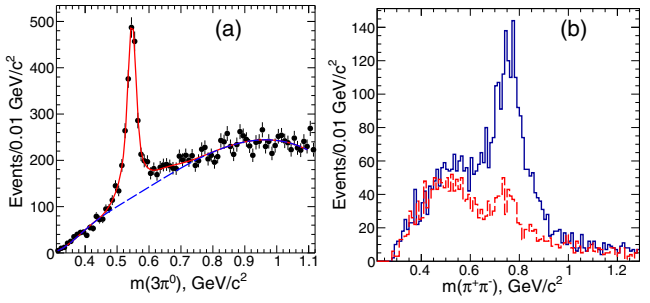

FIG. 15. (a) The $3\pi^0$ invariant mass for data. The curves show the fit functions. The solid curve shows the η peak (based on MC simulation) plus the non-η continuum background (dashed). (b) The $\pi^+\pi^-$ invariant mass for events selected in the η-peak region. The dashed histogram shows the continuum events in the η-peak sidebands.

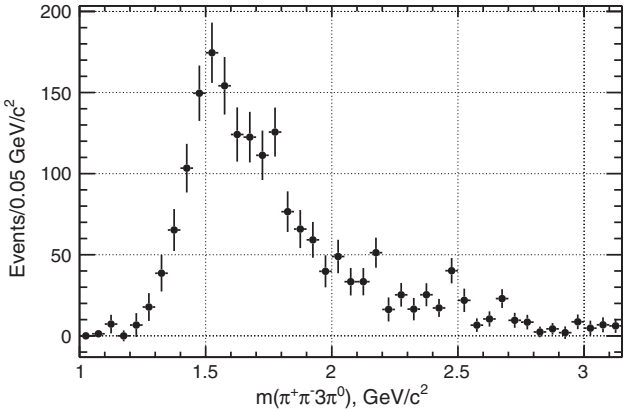

FIG. 16. The $m(\pi^+\pi^-3\pi^0)$ invariant mass dependence of the selected data events for $e^+e^- \to \eta\pi^+\pi^-$, $\eta \to 3\pi^0$.

Using Eq. (1), we determine the cross section for the $e^+e^- \to \eta\pi^+\pi^-$ process. Our simulation takes into account all η decays, so the cross section results shown in Fig. 17(a) and listed in Table III correspond to all η decays.

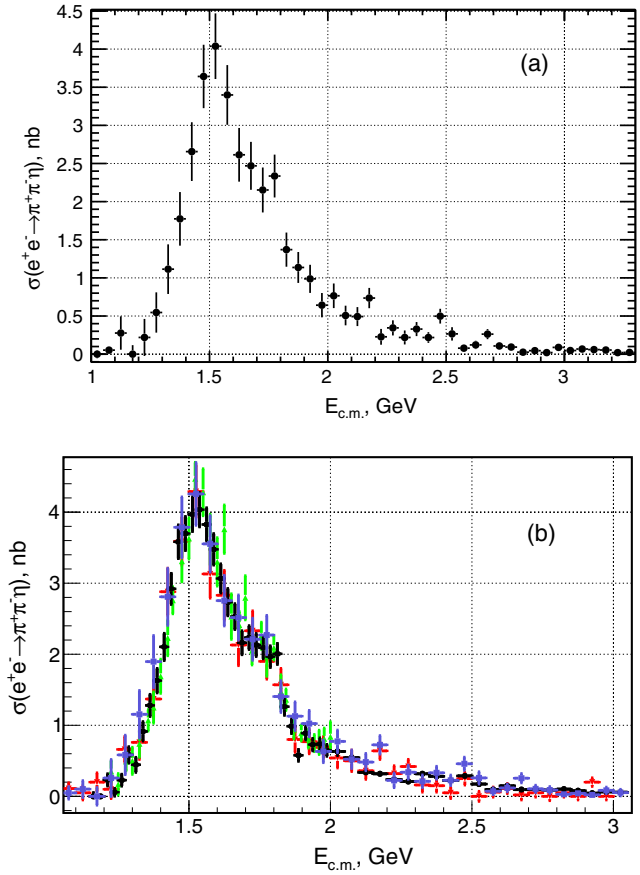

FIG. 17. (a) The energy-dependent $e^+e^- \to \eta\pi^+\pi^-$ cross section obtained in the $2\pi3\pi^0$ mode. (b) Comparison of the current results (squares) with previous measurements from *BABAR* in the $\eta \to \pi^+\pi^-\pi^0$ (upside-down triangles) [14] and $\eta \to \gamma\gamma$ modes (circles) [20]. Results from the SND experiment [31] are shown by triangles.

Systematic uncertainties in this measurement are the same as those listed in Table II. Figure 17(b) shows our measurement in comparison to our previous results [14,20] and to those from the SND experiment [31]. These previous results are based on different η decay modes than that considered here. The different results are seen to agree within the uncertainties. Including the results of the present study, we have thus now measured the $e^+e^- \to \eta\pi^+\pi^-$ cross section in three different η decay modes.

I. The $\omega\pi^0\pi^0$ intermediate state

To determine the contribution of the $\omega\pi^0\pi^0$ intermediate state, we fit the events of Fig. 13(a) using a BW function to model the signal and a polynomial to model the background. The BW function is convoluted with a Gaussian distribution that accounts for the detector resolution, as described for the fit of Fig. 6(b). The result of the fit is shown in Fig. 18(a). We obtain 3960 ± 146 $\omega\pi^0\pi^0$ events. The number of the $\omega\pi^0\pi^0$ events as a function of the five-pion invariant mass is determined by performing an analogous fit of events in Fig. 13(c) in each 0.05 GeV/c^2 interval of $m(\pi^+\pi^-3\pi^0)$. The resulting distribution is shown by the circle symbols in Fig. 18(b). We do not observe a clear $f_0(980) \to \pi^0\pi^0$ signal in the $\pi^0\pi^0$ invariant mass, perhaps because of a large combinatorial background. In contrast, in our previous study of the $e^+e^- \to \omega\pi^+\pi^- \to \pi^+\pi^-\pi^+\pi^-\pi^0$ process [14], a clear $f_0(980) \to \pi^+\pi^-$ signal was seen.

For the $e^+e^- \to \omega\pi^0\pi^0$ channel, there is a peaking background from $e^+e^- \to \omega\pi^0 \to \pi^+\pi^-\pi^0\pi^0$. A simulation of this reaction with proper normalization leads to the peaking-background estimation shown by the square symbols in Fig. 18(b). This background is subtracted from the $\omega\pi^0\pi^0$ signal candidate distribution.

The $e^+e^- \to \omega\pi^0\pi^0$ cross section corrected for the $\omega \to \pi^+\pi^-\pi^0$ branching fraction is shown in Fig. 19 and tabulated in Table IV. The uncertainties are statistical only. The systematic uncertainties are about 10% for $E_{\rm c.m.} < 2.4$ GeV, as discussed in Sec. IV F. No previous measurement exists for this process. The cross section exhibits a rise at threshold, a decrease at large ($E_{\rm c.m.}$,) and a clear resonance at around 1.6 GeV, possibly from the $\omega(1650)$. The measured $e^+e^- \to \omega\pi^0\pi^0$ cross section is around a factor of 2 smaller than that we observed for $e^+e^- \to \omega\pi^+\pi^-$ [14], as is expected from isospin symmetry.

J. The $\rho(770)^\pm\pi^\mp\pi^0\pi^0$ intermediate state

A similar approach is followed to study events with a $\rho^\pm$ meson in the intermediate state. Because the ρ meson is broad, a BW function is used to describe the signal shape. There are six $\rho^\pm$ entries per event, leading to a large combinatoric background. To extract the contribution of the

TABLE III. Summary of the $e^+e^- \to \eta\pi^+\pi^-$ cross section measurement. The uncertainties are statistical only.

$E_{\rm c.m.}$ (GeV)	σ (nb)	$E_{\rm c.m.}$ (GeV)	σ (nb)	$E_{\rm c.m.}$ (GeV)	σ (nb)	$E_{\rm c.m.}$ (GeV)	σ (nb)	$E_{\rm c.m.}$ (GeV)	σ (nb)
1.075	0.06 ± 0.03	1.475	3.74 ± 0.43	1.875	1.16 ± 0.21	2.275	0.35 ± 0.10	2.675	0.27 ± 0.07
1.125	0.29 ± 0.23	1.525	4.14 ± 0.44	1.925	1.00 ± 0.19	2.325	0.22 ± 0.09	2.725	0.11 ± 0.05
1.175	0.00 ± 0.12	1.575	3.48 ± 0.40	1.975	0.65 ± 0.16	2.375	0.33 ± 0.09	2.775	0.09 ± 0.05
1.225	0.23 ± 0.25	1.625	2.67 ± 0.36	2.025	0.78 ± 0.16	2.425	0.22 ± 0.07	2.825	0.03 ± 0.04
1.275	0.57 ± 0.27	1.675	2.52 ± 0.32	2.075	0.51 ± 0.13	2.475	0.51 ± 0.10	2.875	0.05 ± 0.04
1.325	1.15 ± 0.34	1.725	2.20 ± 0.30	2.125	0.50 ± 0.13	2.525	0.27 ± 0.09	2.925	0.02 ± 0.04
1.375	1.83 ± 0.36	1.775	2.38 ± 0.29	2.175	0.75 ± 0.13	2.575	0.08 ± 0.05	2.975	0.09 ± 0.05
1.425	2.74 ± 0.40	1.825	1.39 ± 0.23	2.225	0.23 ± 0.11	2.625	0.12 ± 0.06	3.025	0.05 ± 0.05

$\rho^\pm\pi^\mp\pi^0\pi^0$ intermediate state we fit the events in Fig. 14(a) with a BW function to describe the signal and a polynomial to describe the background. The parameters of the ρ resonance are taken from Ref. [27]. The result of the fit is shown in Fig. 20(a). We obtain 14894 ± 501 $\rho^\pm\pi^\mp\pi^0\pi^0$ events. The distribution of these events vs the five-pion invariant mass is shown by the square symbols in Fig. 21(a).

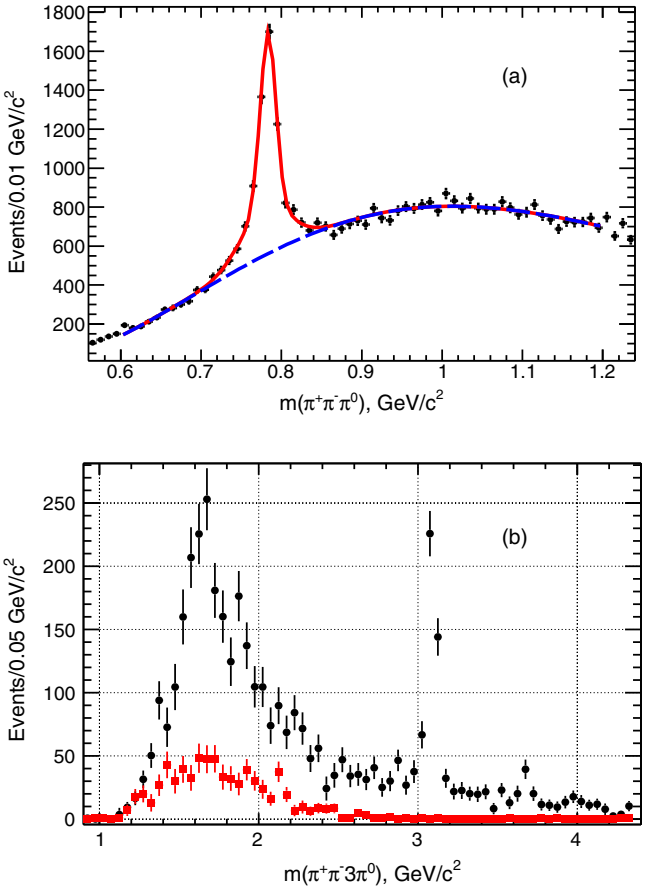

FIG. 18. (a) The $\pi^+\pi^-\pi^0$ invariant mass for data. The solid curve shows the fit function for signal (based on MC simulation) plus the combinatorial background (dashed curve). (b) The mass distribution of the $\pi^+\pi^-3\pi^0$ events in the ω peak (circles) and estimated contribution from the $\omega\pi^0$ background (squares).

The circle symbols in Fig. 21(a) show the total number of $\pi^+\pi^-3\pi^0$ events repeated from Fig. 9. It is seen that the number of events with a $\rho^\pm$ exceeds the total number of $\pi^+\pi^-3\pi^0$ events, implying that there is more than one $\rho^\pm$ per event, namely a significant production of $e^+e^- \to \rho^+\rho^-\pi^0$. To determine the rate of $\rho^+\rho^-\pi^0$ events, we perform a fit to determine the number of ρ^+ in intervals of 0.04 GeV/c^2 in the $\pi^-\pi^0$ distribution of Fig. 14(b). The result is shown in Fig. 20(b). Indeed, a significant ρ^+ peak is observed.

The number of $e^+e^- \to \rho^+\rho^-\pi^0$ events is determined by fitting the data of Fig. 20(b) with the sum of a BW function and a polynomial. The sample is divided into three mass intervals: $m(\pi^+\pi^-3\pi^0) < 2.5$ GeV/(c^2), $2.5 < m(\pi^+\pi^-3\pi^0) < 3.0$ GeV/$((c^2))$, and $m(\pi^+\pi^-3\pi^0) > 3.0$ GeV/(c^2). For each mass interval we determine the number of ρ^+ events. We find that the fraction of correlated $\rho^+\rho^-$ events, relative to the total number of $\pi^+\pi^-3\pi^0$ events with a $\rho^\pm$, decreases with the mass interval as 0.49 ± 0.05, 0.37 ± 0.07, and 0.23 ± 0.10, respectively, where the uncertainties are statistical. Thus, the $\rho^+\rho^-\pi^0$ intermediate state dominates at threshold.

Intermediate states with either one or two $\rho(770)$ are expected to be produced, at least in part, through $e^+e^- \to \rho(1400, 1700)^0\pi^0 \to a_1(1260)^\pm\pi^\mp\pi^0 \to \rho^\pm\pi^\mp\pi^0\pi^0$

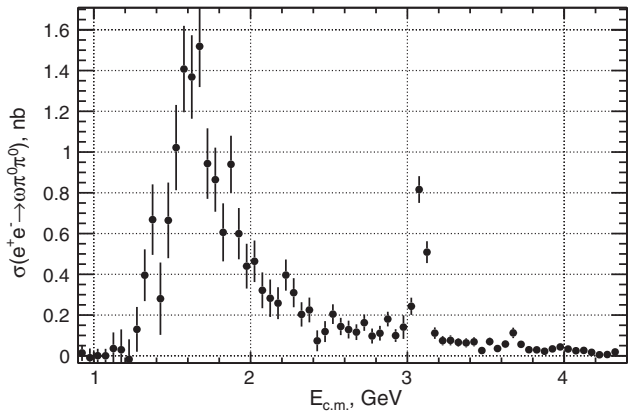

FIG. 19. The energy-dependent $e^+e^- \to \omega\pi^0\pi^0$ cross section in the $\pi^+\pi^-3\pi^0$ mode.

TABLE IV. Summary of the $e^+e^- \to \omega\pi^0\pi^0$ cross section measurement. The uncertainties are statistical only.

$E_{\rm c.m.}$ (GeV)	σ (nb)	$E_{\rm c.m.}$ (GeV)	σ (nb)	$E_{\rm c.m.}$ (GeV)	σ (nb)	$E_{\rm c.m.}$ (GeV)	σ (nb)	$E_{\rm c.m.}$ (GeV)	σ (nb)
1.125	0.04 ± 0.08	1.775	0.88 ± 0.16	2.425	0.07 ± 0.05	3.075	0.83 ± 0.07	3.725	0.06 ± 0.02
1.175	0.03 ± 0.10	1.825	0.62 ± 0.14	2.475	0.12 ± 0.05	3.125	0.52 ± 0.05	3.775	0.03 ± 0.02
1.225	-0.02 ± 0.10	1.875	0.96 ± 0.14	2.525	0.21 ± 0.05	3.175	0.11 ± 0.03	3.825	0.03 ± 0.01
1.275	0.13 ± 0.11	1.925	0.61 ± 0.13	2.575	0.15 ± 0.04	3.225	0.08 ± 0.02	3.875	0.02 ± 0.01
1.325	0.41 ± 0.13	1.975	0.45 ± 0.11	2.625	0.13 ± 0.04	3.275	0.08 ± 0.02	3.925	0.03 ± 0.02
1.375	0.69 ± 0.18	2.025	0.47 ± 0.10	2.675	0.12 ± 0.04	3.325	0.07 ± 0.02	3.975	0.04 ± 0.01
1.425	0.29 ± 0.18	2.075	0.33 ± 0.09	2.725	0.17 ± 0.04	3.375	0.06 ± 0.02	4.025	0.03 ± 0.01
1.475	0.68 ± 0.19	2.125	0.29 ± 0.09	2.775	0.10 ± 0.04	3.425	0.07 ± 0.02	4.075	0.02 ± 0.01
1.525	1.05 ± 0.21	2.175	0.26 ± 0.08	2.825	0.11 ± 0.04	3.475	0.03 ± 0.02	4.125	0.03 ± 0.01
1.575	1.44 ± 0.22	2.225	0.40 ± 0.08	2.875	0.18 ± 0.04	3.525	0.07 ± 0.02	4.175	0.02 ± 0.01
1.625	1.40 ± 0.21	2.275	0.31 ± 0.07	2.925	0.10 ± 0.03	3.575	0.04 ± 0.02	4.225	0.01 ± 0.01
1.675	1.55 ± 0.20	2.325	0.21 ± 0.06	2.975	0.14 ± 0.06	3.625	0.06 ± 0.02	4.275	0.01 ± 0.01
1.725	0.96 ± 0.18	2.375	0.23 ± 0.06	3.025	0.25 ± 0.04	3.675	0.11 ± 0.03	4.325	0.02 ± 0.01

and $e^+e^- \to \rho^\pm a_1^\mp \to \rho^+\rho^-\pi^0$, respectively. Figure 20(c) shows a scatter plot of the $\rho^\pm\pi^0$ invariant mass vs the $\pi^\mp\pi^0$ invariant mass. An indication of the $a_1(1260)$ is seen, but it is not statistically significant.

K. The sum of intermediate states

Figure 21(a) shows the number of $\eta\pi^+\pi^-$ (upside-down triangles), $\omega\pi^0\pi^0$ (triangles), and $\rho^\pm\pi^\mp\pi^0\pi^0$ (square) intermediate state events found as described in the previous sections, in comparison to the total number of $\pi^+\pi^-3\pi^0$ events (circles) found from the fit to the π^0 mass peak. The results for the η and ω are repeated from Figs. 16 and 18, respectively. As noted above, a significant excess of events with a ρ is observed. Based on the results of our study of correlated $\rho^+\rho^-$ production, we scale the number of events found from the fit to the ρ peak so that it corresponds to the number of events with either a single $\rho^\pm$ or with a $\rho^+\rho^-$ pair. We then sum this latter result with the η and ω curves in Fig. 21(a). The result of this sum is shown by the square symbols in Fig. 21(b). This summed curve is seen to be in agreement with the total number of $\pi^+\pi^-3\pi^0$ events shown by the circular symbols.

Note that below $E_{\rm c.m.} = 2$ GeV, the number of events is completely dominated by the $\eta\pi^+\pi^-$ and $\omega\pi^0\pi^0$ channels, so the cross section of the intermediate states with a ρ can be estimated as the difference between the total $e^+e^- \to \pi^+\pi^-\pi^0\pi^0\pi^0$ cross section and the sum of the $\eta\pi^+\pi^-$ and $\omega\pi^0\pi^0$ contributions.

V. THE $\pi^+\pi^-2\pi^0\eta$ FINAL STATE

A. Determination of the number of events

The analogous approach to that described above for $e^+e^- \to \pi^+\pi^-\pi^0\pi^0\pi^0$ events is used to study $e^+e^- \to \pi^+\pi^-\pi^0\pi^0\eta$ events. We fit the η signal in the third-photon-pair invariant mass distribution (cf. Fig. 1) with the sum of two Gaussians with a common mean, while the relatively smooth background is described by a second-order polynomial function, as shown in Fig. 22(a). We obtain 4700 ± 84 events. Figure 22(b) shows the mass distribution of these events.

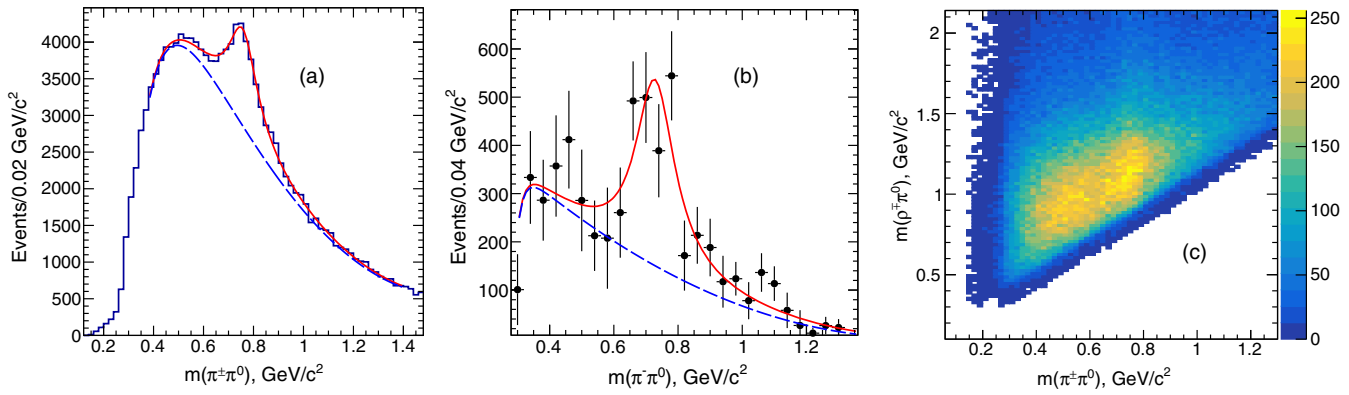

FIG. 20. (a) The $\pi^\pm\pi^0$ invariant mass for data. The dashed curve shows the fit to the combinatorial background. The solid curve is the sum of the background curve and the BW function for the $\rho^\pm$. (b) The result of the ρ^+ fit in bins of 0.04 GeV/c^2 in the ρ^- mass. (c) Scatter plot of the $\rho^\pm\pi^0$ invariant mass vs the $\pi^\mp\pi^0$ invariant mass.

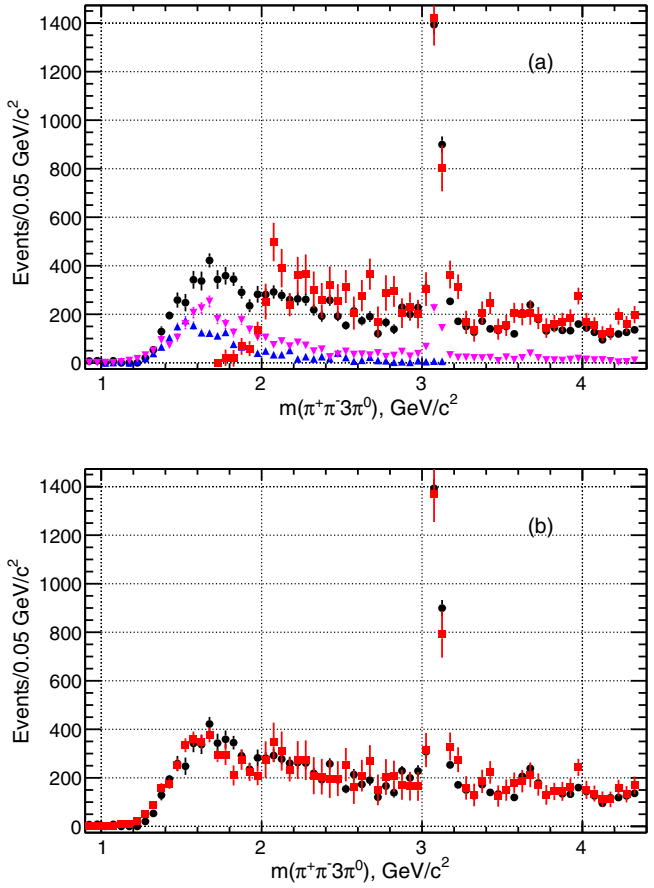

FIG. 21. (a) Number of events in bins of $E_{\mathrm{c.m.}}$ from the $\eta\pi^+\pi^-$ (triangles), $\omega\pi^0\pi^0$ (upside-down triangles), and $\rho \to \pi\pi^0$ (squares) intermediate states. The circles show the total event numbers obtained from the fit to the π^0 peak. (b) The circles are as described for (a). The squares show the sums of event numbers with η, ω and the ρ contribution for correlated $\rho^+\rho^-$ production.

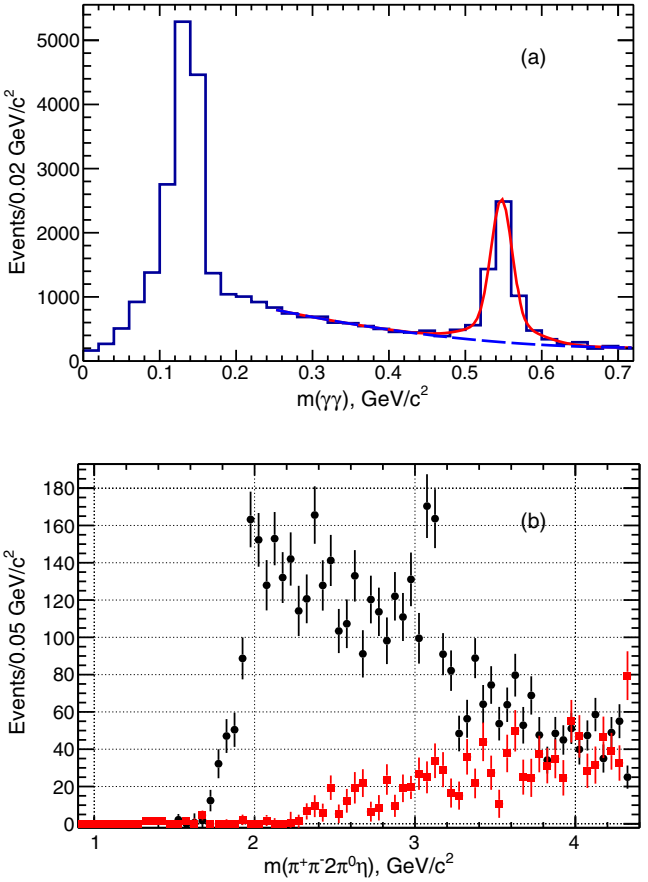

FIG. 22. (a) The third-photon-pair invariant mass for data. The dashed curve shows the fitted background. The solid curve shows the sum of background and the two-Gaussian fit function used to obtain the number of events with an η. (b) The invariant mass distribution for the $\pi^+\pi^-2\pi^0\eta$ events obtained from the η signal fit. The contribution of the *uds* background events is shown by the squares.

B. Peaking background

The major background producing an η peak is the non-ISR background, in particular $e^+e^- \to \pi^+\pi^-\pi^0\pi^0\pi^0\eta$ when one of the neutral pions decays asymmetrically, producing a photon interpreted as ISR. The η peak from the *uds* simulation is visible in Fig. 10.

To normalize the *uds* simulation, we form the diphoton invariant mass distribution of the ISR candidate with all the remaining photons in the event. Comparing the number of events in the π^0 peaks in data and *uds* simulation, we assign a scale factor of 1.5 ± 0.2 to the simulation. We fit the η peak in the *uds* simulation in intervals of 0.05 GeV/c^2 in $m(\pi^+\pi^-\pi^0\pi^0\gamma\gamma)$. The results are shown by the squares in Fig. 22(b).

C. Detection efficiency

We use simulated $e^+e^- \to \pi^+\pi^-\pi^0\pi^0\eta\gamma$ events from the phase space model and with the $\omega\pi^0\eta$ intermediate state to determine the efficiency. As for the data, we fit to find the η signal in the third photon pair in intervals of 0.05 GeV/c^2 in $m(\pi^+\pi^-\pi^0\pi^0\gamma\gamma)$. The fit is illustrated in Fig. 23(a) using all $\pi^+\pi^-\pi^0\pi^0\gamma\gamma$ candidates. The efficiency is determined as the ratio of the number of fitted events in each interval to the number generated in that interval. For the $\omega\pi^0\eta$ intermediate channel, we also determine the efficiency using an alternative method, by fitting the ω peak in the $\pi^+\pi^-\pi^0$ invariant mass distribution shown in Fig. 23(b).

The efficiencies obtained for the three methods are shown in Fig. 24. The circles and squares show the results from the fit to the η peak for the phase space and $\omega\pi^0\eta$ channels, respectively. The triangles show the results for the fit to the ω peak. The efficiencies are calculated assuming the $\eta \to \gamma\gamma$ mode only. The obtained efficiencies are around 4%, similar to what is found for $\pi^+\pi^-3\pi^0$ (Fig. 7). The results from the three methods are consistent with each other, and are averaged. The average is fit with a third-order polynomial shown by the curve in Fig. 24. The result of the fit is used for the cross section determination.

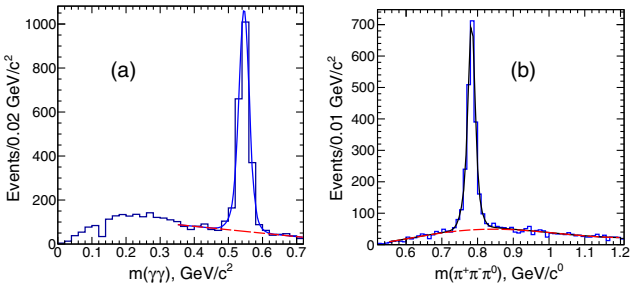

FIG. 23. (a) The third-photon-pair invariant mass for simulation of the $e^+e^- \to \pi^+\pi^-\pi^0\pi^0\eta\gamma$ process. The dashed curve shows the fitted background. The solid curve shows the sum of background and the two-Gaussian fit function used to obtain the number of events with an η. (b) The $\pi^+\pi^-\pi^0$ invariant mass for simulation. The solid curve shows a two-Gaussian fit function for the ω signal plus the combinatorial background (dashed).

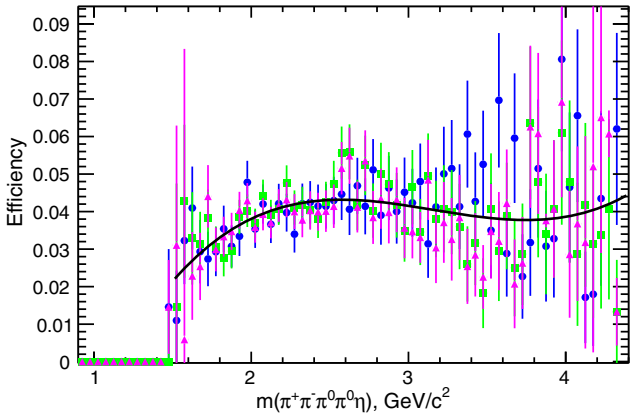

FIG. 24. The energy-dependent detection efficiency determined in three different ways; see text. The curve shows the fit to the average of the three and is used in the cross section determination.

We estimate the systematic uncertainty in the efficiency due to the fit procedure and the model dependence to be not more than 10%.

D. Cross section for $e^+e^- \to \pi^+\pi^-\pi^0\pi^0\eta$

The cross section for $e^+e^- \to \pi^+\pi^-\pi^0\pi^0\eta$ is determined using Eq. (1). The results are shown in Fig. 25 and listed in Table V. These are the first results for this process. The systematic uncertainties and corrections are the same as those presented in Table II except there is an increase in the uncertainty in the detection efficiency. The total systematic uncertainty for $E_{\rm c.m.} < 2.5$ GeV is 13%.

E. Overview of the intermediate structures

The $\pi^+\pi^-2\pi^0\eta$ final state, like that for $\pi^+\pi^-3\pi^0$, has a rich substructure. Figure 26(a) shows the $2\pi^0\eta$ invariant mass distribution for events selected by requiring $|m(\gamma\gamma) - m(\eta)| < 0.07$ GeV/c^2 in Fig. 22(a). There is a small but

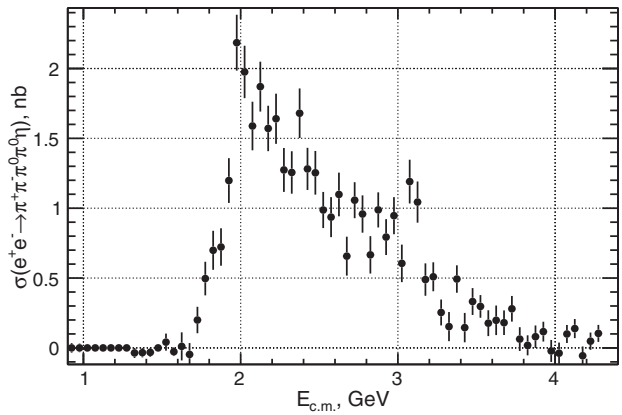

FIG. 25. Energy-dependent cross section for $e^+e^- \to \pi^+\pi^-\pi^0\pi^0\eta$. The uncertainties are statistical only.

clear signal for $\eta(1285)$ production. The dotted histogram shows the background distribution determined using an η sideband control region defined by $0.07 < |m(\gamma\gamma) - m(\eta)| < 0.14\,\text{GeV}/c^2$. Figure 26(b) shows a scatter plot of the $\pi^+\pi^-$ invariant mass vs the $2\pi^0\eta$ invariant mass. No structures are seen.

Figure 27(a) shows the $\pi^+\pi^-\pi^0$ mass distribution (two entries per event). An ω signal is clearly visible, as well as a bump close to 1 GeV/c^2 corresponding to $\phi \to \pi^+\pi^-\pi^0$. The dotted histogram shows the estimate of the background evaluated using the η sideband described above. The scatter plot in Fig. 27(b) shows the $\pi^0\eta$ vs the $\pi^+\pi^-\pi^0$ invariant mass. A clear correlation of ω and $a_0(980) \to \pi^0\eta$ production is seen. Figure 27(c) shows how $\omega\pi^0\eta$ events are distributed over the $\pi^+\pi^-2\pi^0\eta$ invariant mass.

Figure 28(a) presents the $\pi^+\pi^0$ (solid) and $\pi^-\pi^0$ (dotted) mass combinations (two entries per event) for the selected $\pi^+\pi^-2\pi^0\eta$ events. Signals from the $\rho^\pm$ are clearly visible, but they can also come from events with a $\rho^+\rho^-$ pair. The fraction of $\rho^+\rho^-$ events is extracted from the distribution in Fig. 28(b), where the $\pi^+\pi^0$ vs the $\pi^-\pi^0$ invariant mass is shown. Figure 28(c) displays the $\pi^\pm\pi^0$ vs the $\pi^+\pi^-2\pi^0\eta$ invariant mass.

F. The $\omega\pi^0\eta$ and $\phi\pi^0\eta$ intermediate states

To determine the contribution of the $\omega\pi^0\eta$ and $\phi\pi^0\eta$ intermediate states, we fit the events in Fig. 27(a) with two Gaussian functions, one to describe the ω peak and the other the ϕ peak, and a polynomial function, which describes the background. The results of the fit are shown in Fig. 29(a). We obtain 1676 ± 22 and 269 ± 68 events for the ω and ϕ, respectively. The number of events as a function of the $\pi^+\pi^-2\pi^0\eta$ invariant mass is determined by performing an analogous fit of events in Fig. 27(c) in intervals of 0.05 GeV/c^2 in $m(\pi^+\pi^-2\pi^0\eta)$.

We select events within ± 0.7 GeV/c^2 of the ω peak in Fig. 29(a) and display the resulting $\pi^0\eta$ invariant mass in

TABLE V. Summary of the $e^+e^- \to \pi^+\pi^-\pi^0\pi^0\eta$ cross section measurement. The uncertainties are statistical only.

$E_{\text{c.m.}}$ (GeV)	σ (nb)	$E_{\text{c.m.}}$ (GeV)	σ (nb)	$E_{\text{c.m.}}$ (GeV)	σ (nb)	$E_{\text{c.m.}}$ (GeV)	σ (nb)	$E_{\text{c.m.}}$ (GeV)	σ (nb)
1.625	0.01 ± 0.10	2.175	1.59 ± 0.16	2.725	1.07 ± 0.13	3.275	0.26 ± 0.09	3.825	0.02 ± 0.07
1.675	-0.05 ± 0.08	2.225	1.66 ± 0.18	2.775	0.97 ± 0.14	3.325	0.15 ± 0.11	3.875	0.08 ± 0.08
1.725	0.20 ± 0.10	2.275	1.29 ± 0.16	2.825	0.68 ± 0.14	3.375	0.50 ± 0.10	3.925	0.12 ± 0.07
1.775	0.51 ± 0.12	2.325	1.27 ± 0.15	2.875	1.00 ± 0.13	3.425	0.15 ± 0.11	3.975	-0.02 ± 0.08
1.825	0.71 ± 0.14	2.375	1.70 ± 0.18	2.925	0.81 ± 0.13	3.475	0.34 ± 0.10	4.025	-0.04 ± 0.08
1.875	0.73 ± 0.14	2.425	1.30 ± 0.15	2.975	0.96 ± 0.13	3.525	0.30 ± 0.08	4.075	0.10 ± 0.06
1.925	1.22 ± 0.16	2.475	1.27 ± 0.16	3.025	0.61 ± 0.14	3.575	0.18 ± 0.09	4.125	0.14 ± 0.07
1.975	2.22 ± 0.20	2.525	1.00 ± 0.13	3.075	1.21 ± 0.16	3.625	0.20 ± 0.11	4.175	-0.06 ± 0.07
2.025	2.01 ± 0.19	2.575	0.95 ± 0.15	3.125	1.06 ± 0.15	3.675	0.18 ± 0.09	4.225	0.05 ± 0.06
2.075	1.61 ± 0.18	2.625	1.11 ± 0.16	3.175	0.50 ± 0.12	3.725	0.28 ± 0.09	4.275	0.10 ± 0.06
2.125	1.90 ± 0.18	2.675	0.67 ± 0.14	3.225	0.52 ± 0.11	3.775	0.06 ± 0.09	4.325	0.04 ± 0.06

Fig. 29(b). A very clear signal from the $a_0(980)$ is observed, while no signal is seen in an ω sideband defined by $0.07 < |m(\pi^+\pi^-\pi^0) - m(\omega)| < 0.14$ GeV/c^2.

The obtained $e^+e^- \to \omega\pi^0\eta$ cross section corrected for the $\omega \to \pi^+\pi^-\pi^0$ branching fraction is shown in Fig. 30 in comparison to previous results from SND [32]. The SND results, which are available only for energies below 2 GeV, are seen to lie systematically above our data. All systematic uncertainties discussed in Sec. IV F are applied to the measured $e^+e^- \to \omega\pi^0\eta$ cross section, resulting in a total systematic uncertainty of 13% below 2.4 GeV. The results are presented in Table VI (statistical uncertainties only) in

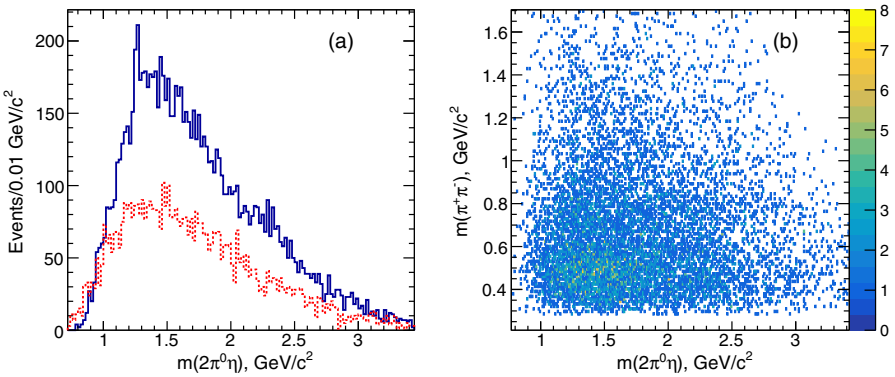

FIG. 26. (a) The $2\pi^0\eta$ invariant mass of the selected $\pi^+\pi^-2\pi^0\eta$ events (solid histogram), and the background determined from the χ^2 sideband (dotted histogram). (b) The $\pi^+\pi^-$ vs the $2\pi^0\eta$ mass for the selected events.

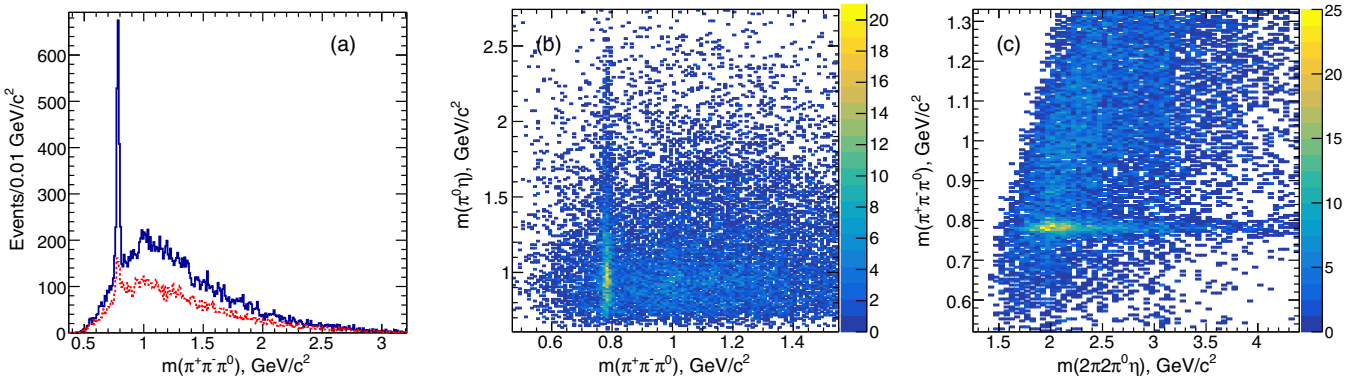

FIG. 27. (a) The $\pi^+\pi^-\pi^0$ invariant mass with two entries per event (solid histogram) and the background estimate from the η sideband (dotted histogram). (b) The $\pi^0\eta$ vs the $\pi^+\pi^-\pi^0$ invariant mass. (c) The $\pi^+\pi^-\pi^0$ invariant mass vs the $\pi^+\pi^-2\pi^0\eta$ invariant mass.

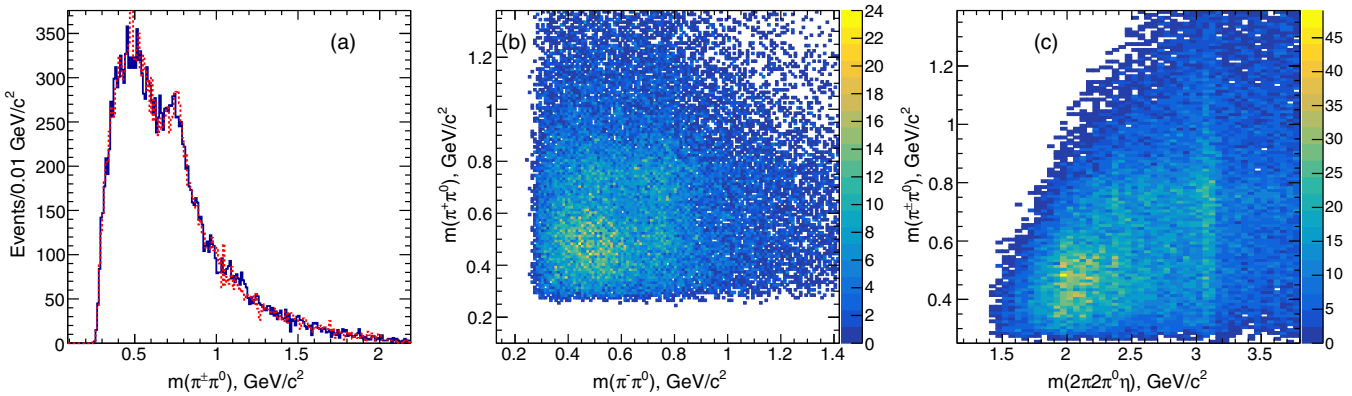

FIG. 28. (a) The $\pi^+\pi^0$ (solid) and $\pi^-\pi^0$ (dotted) invariant mass for the selected $\pi^+\pi^-2\pi^0\eta$ events (two entries per event). (b) The $\pi^-\pi^0$ vs the $\pi^+\pi^0$ invariant mass for the selected events. (c) The $\pi^\pm\pi^0$ invariant mass vs the $\pi^+\pi^-2\pi^0\eta$ invariant mass.

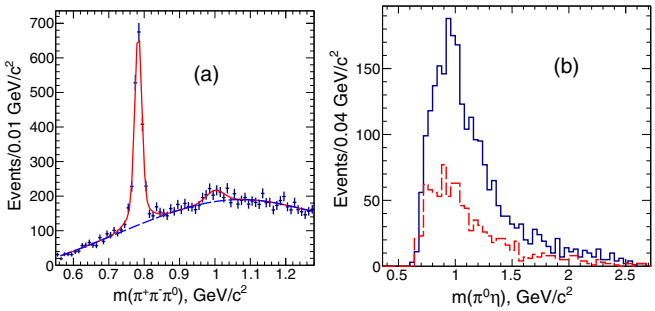

FIG. 29. (a) The $\pi^+\pi^-\pi^0$ invariant mass for the data. The dashed curve describes the nonresonant background. The solid curve shows the sum of the background and the fit functions for the ω and ϕ contributions described in the text. (b) The $\pi^0\eta$ invariant mass distribution for the events selected in the ω peak (solid). The dashed histogram shows the distribution from the ω-peak sideband.

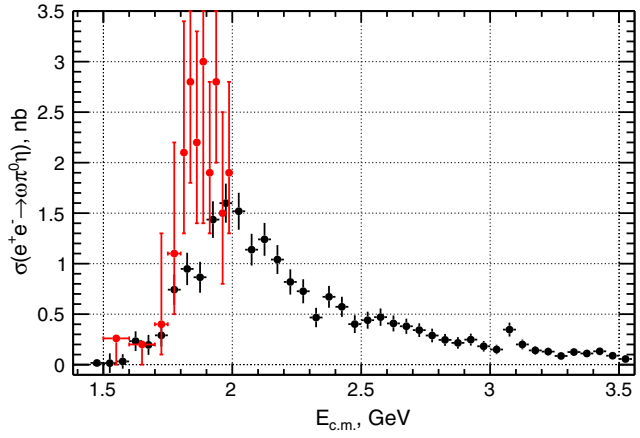

FIG. 30. The $E_{\text{c.m.}}$ dependence of the $e^+e^- \to \omega\pi^0\eta$ cross section (circles) in comparison with the SND results [32] (squares).

bin widths of 0.05 GeV. Above 3.5 GeV, the cross section measurements are consistent with zero within the experimental accuracy.

G. The $\rho(770)^\pm\pi^\mp\pi^0\eta$ intermediate state

The approach described in Sec. IV J is used to study events with a $\rho^\pm$ meson in the intermediate state. We fit the events in Fig. 28(a) using a BW function to describe the ρ signal and a polynomial function to describe the background (four entries per event). The fit yields 2908 ± 202 $\rho^\pm\pi^\mp\pi^0\eta$ events. The result of the fit is shown in Fig. 31(a). The distribution of these events vs the $\pi^+\pi^-2\pi^0\eta$ invariant mass is shown by the squares in Fig. 32.

The size of our data sample is not sufficient to justify a sophisticated amplitude analysis, as would be needed to extract detailed information on all the intermediate states. We can deduce that an intermediate $a_0(980)\rho\pi$ state is present: a correlated bump at the $a_0(980)$ and ρ invariant masses is seen in the scatter plot of Fig. 31(b), where the $\pi^\pm\eta$ invariant mass is plotted vs the $\pi^\mp\pi^0$ mass. Also, there is a contribution from $\rho^+\rho^-\eta$: a scatter plot of the $\pi^\pm\pi^0$ vs the $\pi^\mp\pi^0$ invariant mass is presented in Fig. 28(b), from which an enhancement corresponding to correlated $\rho^+\rho^-$ production is visible.

H. The sum of intermediate states

Figure 32 displays the number of events obtained from the fits described above to the ω (triangles), ϕ (upside-down triangles), and ρ (square) peaks. The results are shown in comparison to the total number of $\pi^+\pi^-2\pi^0\eta$ events (circles) obtained from the fit to the third-photon-pair invariant mass distribution. The sum of events from the intermediate states is seen to agree within the uncertainties with the total number of $\pi^+\pi^-2\pi^0\eta$ events, except in the region around 2 GeV.

TABLE VI. Summary of the $e^+e^- \to \omega\pi^0\eta$ cross section measurement. The uncertainties are statistical only.

$E_{\rm c.m.}$ (GeV)	σ (nb)	$E_{\rm c.m.}$ (GeV)	σ (nb)	$E_{\rm c.m.}$ (GeV)	σ (nb)	$E_{\rm c.m.}$ (GeV)	σ (nb)	$E_{\rm c.m.}$ (GeV)	σ (nb)
1.525	0.02 ± 0.10	2.125	1.26 ± 0.17	2.725	0.35 ± 0.07	3.325	0.13 ± 0.04	3.925	0.08 ± 0.03
1.575	0.03 ± 0.07	2.175	1.06 ± 0.14	2.775	0.29 ± 0.07	3.375	0.11 ± 0.03	3.975	0.00 ± 0.03
1.625	0.24 ± 0.10	2.225	0.83 ± 0.13	2.825	0.25 ± 0.06	3.425	0.13 ± 0.04	4.025	0.05 ± 0.02
1.675	0.20 ± 0.10	2.275	0.74 ± 0.12	2.875	0.22 ± 0.06	3.475	0.09 ± 0.03	4.075	0.00 ± 0.03
1.725	0.30 ± 0.11	2.325	0.47 ± 0.10	2.925	0.25 ± 0.06	3.525	0.06 ± 0.03	4.125	0.04 ± 0.02
1.775	0.76 ± 0.15	2.375	0.68 ± 0.11	2.975	0.18 ± 0.05	3.575	0.10 ± 0.03	4.175	0.03 ± 0.02
1.825	0.96 ± 0.16	2.425	0.58 ± 0.10	3.025	0.15 ± 0.05	3.625	0.02 ± 0.02	4.225	0.03 ± 0.02
1.875	0.88 ± 0.16	2.475	0.41 ± 0.09	3.075	0.35 ± 0.07	3.675	0.06 ± 0.03	4.275	0.00 ± 0.03
1.925	1.46 ± 0.18	2.525	0.45 ± 0.09	3.125	0.20 ± 0.05	3.725	0.05 ± 0.03	4.325	0.02 ± 0.01
1.975	1.62 ± 0.20	2.575	0.48 ± 0.09	3.175	0.14 ± 0.04	3.775	0.08 ± 0.02		
2.025	1.54 ± 0.19	2.625	0.41 ± 0.08	3.225	0.13 ± 0.04	3.825	0.04 ± 0.03		
2.075	1.16 ± 0.16	2.675	0.39 ± 0.08	3.275	0.09 ± 0.03	3.875	0.07 ± 0.02		

VI. THE J/ψ REGION

A. The $\pi^+\pi^-3\pi^0$ final state

Figure 33(a) shows an expanded view of the J/ψ mass region from Fig. 9 for the five-pion data sample. Signals from $J/\psi \to \pi^+\pi^-\pi^0\pi^0\pi^0$ and $\psi(2S) \to \pi^+\pi^-\pi^0\pi^0\pi^0$ are clearly seen. The nonresonant background distribution is flat in this region.

The observed peak shapes are not purely Gaussian because of radiation effects and resolution, as is also seen in the simulated signal distributions shown in Fig. 33(b). The sum of two Gaussians with a common mean is used to describe them. We obtain 2389 ± 63 J/ψ events and 177 ± 27 $\psi(2S)$ events. Using the results for the number of events, the detection efficiency, and the ISR luminosity, we determine the product:

$$B_{J/\psi\to 5\pi}\cdot\Gamma_{ee}^{J/\psi} = \frac{N(J/\psi \to \pi^+\pi^-3\pi^0)\cdot m_{J/\psi}^2}{6\pi^2\cdot d\mathcal{L}/dE\cdot\epsilon^{\rm MC}\cdot\epsilon^{\rm corr}\cdot C} = (150 \pm 4 \pm 15)\ {\rm eV}, \quad (2)$$

where $\Gamma_{ee}^{J/\psi}$ is the electronic width, $d\mathcal{L}/dE = 180\,{\rm nb}^{-1}/{\rm MeV}$ is the ISR luminosity at the J/ψ mass $m_{J/\psi}$, $\epsilon^{\rm MC} = 0.041$ is the detection efficiency from simulation with the corrections $\epsilon^{\rm corr} = 0.88$ discussed in Sec. IV F, and $C = 3.894 \times 10^{11}$ nb MeV^2 is a conversion constant [27]. We estimate the systematic uncertainty for this region to be 10%, because no background subtraction is needed. The subscript "5π" for

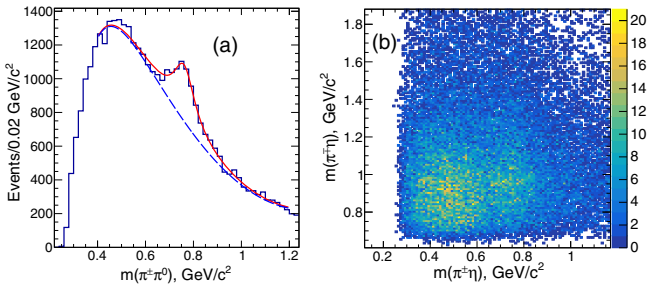

FIG. 31. (a) The $\pi^\pm\pi^0$ invariant mass for data. The curves show the fit functions described in the text. (b) The $\pi^\pm\eta$ vs the $\pi^\mp\pi^0$ invariant mass.

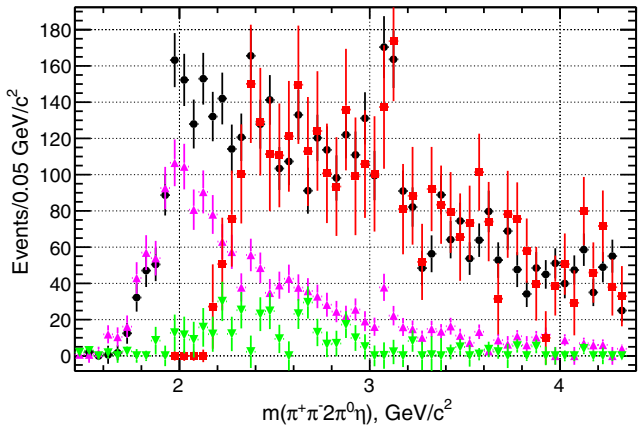

FIG. 32. Number of events in bins of $E_{\rm c.m.}$ for inclusive $\pi^+\pi^-2\pi^0\eta$ events (circles) and for the $\omega\pi^0\eta$ (triangles), $\phi\pi^0\eta$ (upside-down triangles), and $\rho^\pm\pi^\mp\pi^0\eta$ (squares) intermediate states.

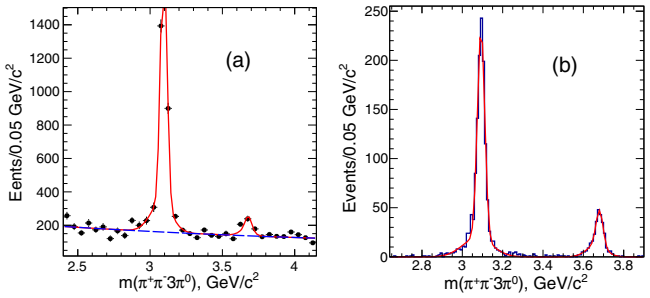

FIG. 33. (a) The $\pi^+\pi^-3\pi^0$ mass distribution for ISR-produced $e^+e^- \to \pi^+\pi^-\pi^0\pi^0\pi^0$ events in the J/ψ–$\psi(2S)$ region. (b) The MC-simulated signals. The curves show the fit functions described in the text.

the branching fraction refers to the $\pi^+\pi^-3\pi^0$ final state exclusively.

Using $\Gamma_{ee}^{J/\psi} = 5.55 \pm 0.14\,\text{keV}$ [27], we obtain $B_{J/\psi\to 5\pi} = (2.70 \pm 0.07 \pm 0.27) \times 10^{-2}$: no other measurements for this channel exist.

Using Eq. (2) and the result $d\mathcal{L}/dE = 228\ \text{nb}^{-1}/\text{MeV}$ at the $\psi(2S)$ mass, we obtain

$$B_{\psi(2S)\to 5\pi} \cdot \Gamma_{ee}^{\psi(2S)} = (12.4 \pm 1.9 \pm 1.2)\ \text{eV}.$$

With $\Gamma_{ee}^{\psi(2S)} = 2.34 \pm 0.06$ keV [27] we find $B_{\psi(2S)\to 5\pi} = (5.2 \pm 0.8 \pm 0.5) \times 10^{-3}$. For this channel also, no previous result exists.

The $\psi(2S)$ peak partly corresponds to the decay chain $\psi(2S) \to J/\psi\pi^0\pi^0 \to \pi^+\pi^-\pi^0\pi^0\pi^0$, with J/ψ decay to three pions. We select the $\pi^+\pi^-\pi^0$ mass combination closest to the J/ψ mass. Figure 34(a) displays this $\pi^+\pi^-\pi^0$ mass vs the five-pion invariant mass. A clear signal from the above decay chain is seen. We select events in a $\pm 0.05\ \text{GeV}/c^2$ window around the J/ψ mass and project the results onto $m(\pi^+\pi^-3\pi^0)$. The results are shown in Fig. 34(b). Performing a fit to this distribution yields 142 ± 21 $\psi(2S) \to J/\psi\pi^0\pi^0 \to \pi^+\pi^-\pi^0\pi^0\pi^0$ events. In conjunction with the detection efficiency and ISR luminosity, this yields

$$B_{\psi(2S)\to J/\psi\pi^0\pi^0} \cdot B_{J/\psi\to\pi^+\pi^-\pi^0} \cdot \Gamma_{ee}^{\psi(2S)} = (10.1 \pm 1.5 \pm 1.1)\ \text{eV}.$$

With $\Gamma_{ee}^{\psi(2S)}$ as stated above and $B_{\psi(2S)\to J/\psi\pi^0\pi^0} = 0.1817 \pm 0.0031$ [27], we obtain $B_{J/\psi\to\pi^+\pi^-\pi^0} = (2.29 \pm 0.28 \pm 0.23)\%$, in agreement with our direct measurement $B_{J/\psi\to\pi^+\pi^-\pi^0} = (2.18 \pm 0.19)\%$ [13] as well as with the Particle Data Group (PDG) value $B_{J/\psi\to\pi^+\pi^-\pi^0} = (2.11 \pm 0.07)\%$. This gives us confidence that our normalization procedure is correct.

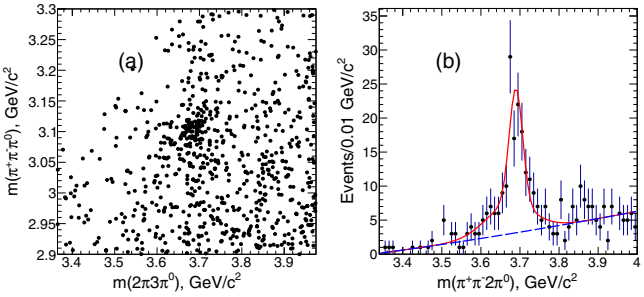

FIG. 34. (a) The three-pion combination closest to the J/ψ mass vs the five-pion mass. (b) The five-pion mass for the events with the three-pion mass in the $\pm 50\ \text{MeV}/c^2$ interval around the J/ψ mass. The curves show the fit functions for all events (solid) and the contribution of the background (dashed).

1. The $\omega\pi^0\pi^0$ intermediate state

The $J/\psi \to \eta\pi^+\pi^-$ branching fraction is very small, as we observed in our previous publication [20], and there is not a statistically significant signal in our sample shown in Fig. 16. We do not attempt to extract a J/ψ branching fraction for this channel.

Figure 35(a) shows an expanded view of Fig. 18 with the $\pi^+\pi^-3\pi^0$ mass distribution for events obtained by a fit to the $\pi^+\pi^-\pi^0$ mass distribution. The two-Gaussian fit implemented as described above yields 398 ± 29 and 33 ± 10 events for the J/ψ and $\psi(2S)$, respectively. Using Eq. (2) we obtain

$$B_{J/\psi\to\omega\pi^0\pi^0} \cdot B_{\omega\to\pi^+\pi^-\pi^0} \cdot \Gamma_{ee}^{J/\psi} = (24.9 \pm 1.8 \pm 2.5)\ \text{eV},$$
$$B_{\psi(2S)\to\omega\pi^+\pi^-} \cdot B_{\omega\to\pi^+\pi^-\pi^0} \cdot \Gamma_{ee}^{\psi(2S)} = (2.3 \pm 0.7 \pm 0.2)\ \text{eV}.$$

Using $B_{\omega\to\pi^+\pi^-\pi^0} = 0.891$ and the value of Γ_{ee} from Ref. [27], we obtain $B_{J/\psi\to\omega\pi^0\pi^0} = (5.04 \pm 0.37 \pm 0.50) \times 10^{-3}$ and $B_{\psi(2S)\to\omega\pi^0\pi^0} = (1.1 \pm 0.3 \pm 0.1) \times 10^{-3}$. The value of $B_{J/\psi\to\omega\pi^0\pi^0}$ listed in Ref. [27] based on the DM2 [33] result is $(3.4 \pm 0.8) \times 10^{-3}$. There is no previous result for $B_{\psi(2S)\to\omega\pi^0\pi^0}$. Note that our result for $B_{J/\psi\to\omega\pi^0\pi^0}$ is about a factor of 2 lower than our result $B_{J/\psi\to\omega\pi^+\pi^-} = (9.7 \pm 0.9) \times 10^{-3}$ [14], as expected from isospin symmetry.

2. The $\rho^\pm\pi^\mp\pi^0\pi^0$ intermediate state

Figure 35(b) shows an expanded view of Fig. 21(a) (squares) for the $\pi^+\pi^-3\pi^0$ mass, for events obtained from the fit to the ρ signal in the $\pi^\pm\pi^0$ mass. The two-Gaussian fit yields 2299 ± 201 and < 88 events at 90% C.L. for the J/ψ and $\psi(2S)$, respectively.

The obtained $J/\psi \to \rho^\pm\pi^\mp\pi^0\pi^0$ result exceeds the total number of observed J/ψ events. This is because of J/ψ decays to $\rho^+\rho^-\pi^0$. Figure 36(a) shows a scatter plot of the $\pi^+\pi^0$ vs the $\pi^-\pi^0$ invariant mass for 3051 events in a $\pm 0.1\ \text{GeV}/c^2$ interval around the J/ψ peak of Fig. 35(b).

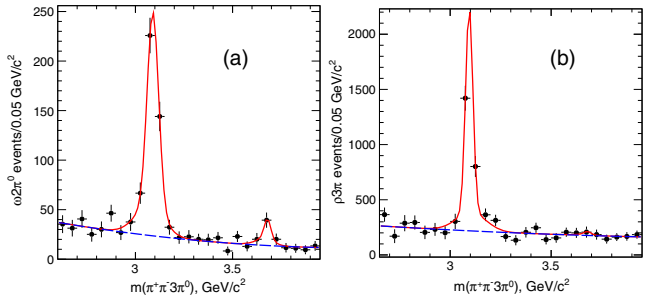

FIG. 35. (a) The five-pion mass for events with the three-pion combination in the $\omega(782)$ mass region. (b) The five-pion mass for events with $\pi^\pm\pi^0$ combination in the $\rho(770)$ mass region. The curves show the fit functions described in the text.

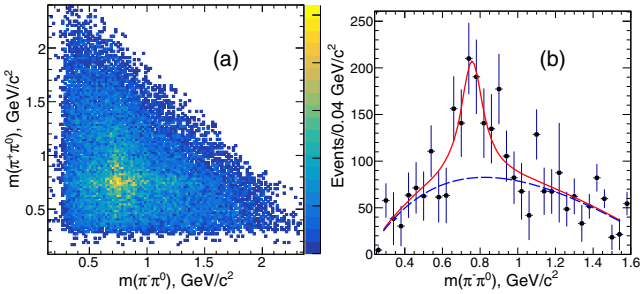

FIG. 36. (a) Scatter plot of the $\pi^+\pi^0$ vs the $\pi^-\pi^0$ invariant mass for the J/ψ region in Fig. 35(b). (b) Number of $\pi^+\pi^0$ events in bins of 0.04 GeV/c^2 in the $\pi^-\pi^0$ mass. The curves show the fit functions for all events (solid) and the contribution of the background (dashed).

To determine the rate of correlated $\rho^+\rho^-$ production, we fit the $\pi^+\pi^0$ invariant mass with a BW and combinatorial background function in intervals of 0.04 GeV/c^2 in the $\pi^-\pi^0$ mass distribution. The resulting distribution exhibits a clear ρ peak shown in Fig. 36(b), with a correlated $\rho^+\rho^-$ yield of 703 ± 153 events, corresponding to $46 \pm 8\%$ of the $\rho^\pm\pi^\mp\pi^0\pi^0$ events. Using this value we estimate the number of J/ψ decays to single and double ρ to be $1241 \pm 109 \pm 183$ and $529 \pm 46 \pm 92$, respectively. The second uncertainty is from the uncertainty in the fraction of $\rho^+\rho^-$ events given above. We obtain

$$B_{J/\psi\to\rho^\pm\pi^\mp\pi^0\pi^0}\cdot\Gamma_{ee}^{J/\psi} = (78 \pm 7 \pm 8 \pm 6)\ \text{eV},$$
$$B_{J/\psi\to\rho^+\rho^-\pi^0}\cdot\Gamma_{ee}^{J/\psi} = (33 \pm 3 \pm 3 \pm 3)\ \text{eV}.$$

Dividing by the value of Γ_{ee} from Ref. [27] then yields

$$B_{J/\psi\to\rho^\pm\pi^\mp\pi^0\pi^0} = (1.40 \pm 0.12 \pm 0.14 \pm 0.10)\times 10^{-2},$$
$$B_{J/\psi\to\rho^+\rho^-\pi^0} = (0.60 \pm 0.05 \pm 0.06 \pm 0.05)\times 10^{-2},$$

where the third uncertainty is associated with the uncertainty arising from the procedure used to determine the correlated $\rho^+\rho^-$ rate. No other measurements for these processes exist.

B. The $\pi^+\pi^-2\pi^0\eta$ final state

Figure 37 shows an expanded view of Fig. 32, with a clear J/ψ signal seen in all three distributions: the inclusive $\pi^+\pi^-2\pi^0\eta$ mass distribution [Fig. 37(a)] and the mass distributions for the $\omega\pi^0\eta$ [Fig. 37(b)] and $\rho^\pm\pi^\mp\pi^0\eta$ [Fig. 37(c)] intermediate states. Our fits yield 203 ± 29, 27 ± 14, and 168 ± 62 events for the J/ψ decays into these final states, respectively. Only an upper limit with < 12 events at 90% C.L. is obtained for the $\psi(2S)$ decay to $\pi^+\pi^-2\pi^0\eta$. We determine

$$B_{J/\psi\to\pi^+\pi^-\pi^0\pi^0\eta}\cdot\Gamma_{ee}^{J/\psi} = (12.8 \pm 1.8 \pm 2.0)\ \text{eV},$$
$$B_{J/\psi\to\omega\pi^0\eta}\cdot B_{\omega\to3\pi}\cdot\Gamma_{ee}^{J/\psi} = (1.7 \pm 0.8 \pm 0.3)\ \text{eV},$$
$$B_{J/\psi\to\rho^\pm\pi^\mp\pi^0\eta}\cdot\Gamma_{ee}^{J/\psi} = (10.5 \pm 4.1 \pm 1.6)\ \text{eV},$$
$$B_{\psi(2S)\to\pi^+\pi^-\pi^0\pi^0\eta}\cdot\Gamma_{ee}^{\psi(2S)} < 0.85\ \text{eV} \quad \text{at} \quad 90\%\text{C.L.}$$

Dividing by the appropriate Γ_{ee} value from Ref. [27], we find $B_{J/\psi\to\pi^+\pi^-\pi^0\pi^0\eta} = (2.30 \pm 0.33 \pm 0.35)\times 10^{-3}$, $B_{J/\psi\to\omega\pi^0\eta} = (3.4 \pm 1.6 \pm 0.6)\times 10^{-4}$, $B_{J/\psi\to\rho^\pm\pi^\mp\pi^0\eta} = (1.9\pm0.7\pm0.3)\times10^{-3}$, and $B_{\psi(2S)\to\pi^+\pi^-\pi^0\pi^0\eta} < 3.5\times10^{-4}$ at 90% C.L. There are no previous results for these final states.

C. Summary of the charmonium region study

The rates of J/ψ and $\psi(2S)$ decays to $\pi^+\pi^-3\pi^0$, $\pi^+\pi^-2\pi^0\eta$ and several intermediate final states have been measured. A small discrepancy with only one available current PDG value measured by the DM2 experiment [33] is observed for the $J/\psi \to \omega\pi^0\pi^0$ decay rate. The measured products and calculated branching fractions are summarized in Table VII together with the available PDG values for comparison.

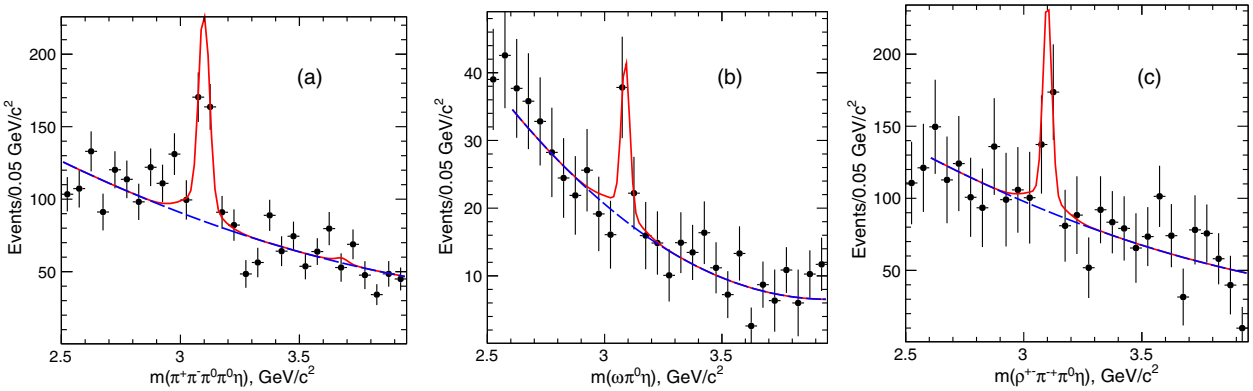

FIG. 37. The J/ψ region for the (a) $\pi^+\pi^-2\pi^0\eta$, (b) $\omega\pi^0\eta$, and (c) $\rho^\pm\pi^\mp\pi^0\eta$ events. The curves show the fit functions described in the text.

TABLE VII. Summary of the J/ψ and $\psi(2S)$ branching fractions.

		J/ψ or $\psi(2S)$ branching fraction (10^{-3})	
Measured quantity	Measured value (eV)	Calculated, this work	PDG [27]
$\Gamma_{ee}^{J/\psi} \cdot \mathcal{B}_{J/\psi\to\pi^+\pi^-\pi^0\pi^0\pi^0}$	$150.0 \pm 4.0 \pm 15.0$	$27.0 \pm 0.7 \pm 2.7$	No entry
$\Gamma_{ee}^{J/\psi} \cdot \mathcal{B}_{J/\psi\to\omega\pi^0\pi^0} \cdot \mathcal{B}_{\omega\to3\pi}$	$24.8 \pm 1.8 \pm 2.5$	$5.04 \pm 0.37 \pm 0.50$	3.4 ± 0.8
$\Gamma_{ee}^{J/\psi} \cdot \mathcal{B}_{J/\psi\to\rho^\pm\pi^\mp\pi^0\pi^0}$	$78.0 \pm 9.0 \pm 8.0$	$14.0 \pm 1.2 \pm 1.4$	No entry
$\Gamma_{ee}^{J/\psi} \cdot \mathcal{B}_{J/\psi\to\rho^+\rho^-\pi^0}$	$33.0 \pm 5.0 \pm 3.3$	$6.0 \pm 0.9 \pm 0.6$	No entry
$\Gamma_{ee}^{J/\psi} \cdot \mathcal{B}_{J/\psi\to\pi^+\pi^-\pi^0\pi^0\eta}$	$12.8 \pm 1.8 \pm 2.0$	$2.30 \pm 0.33 \pm 0.35$	No entry
$\Gamma_{ee}^{J/\psi} \cdot \mathcal{B}_{J/\psi\to\omega\pi^0\eta} \cdot \mathcal{B}_{\omega\to3\pi}$	$1.7 \pm 0.8 \pm 0.3$	$0.34 \pm 0.16 \pm 0.06$	No entry
$\Gamma_{ee}^{J/\psi} \cdot \mathcal{B}_{J/\psi\to\rho^\pm\pi^\mp\pi^0\eta}$	$10.5 \pm 4.1 \pm 1.6$	$1.7 \pm 0.7 \pm 0.3$	No entry
$\Gamma_{ee}^{\psi(2S)} \cdot \mathcal{B}_{\psi(2S)\to\pi^+\pi^-\pi^0\pi^0\pi^0}$	$12.4 \pm 1.8 \pm 1.2$	$5.2 \pm 0.8 \pm 0.5$	No entry
$\Gamma_{ee}^{\psi(2S)} \cdot \mathcal{B}_{\psi(2S)\to J/\psi\pi^0\pi^0} \cdot \mathcal{B}_{J/\psi\to3\pi}$	$10.1 \pm 1.5 \pm 1.1$	$22.9 \pm 2.8 \pm 2.3$	21.1 ± 0.7
$\Gamma_{ee}^{\psi(2S)} \cdot \mathcal{B}_{\psi(2S)\to\omega\pi^0\pi^0} \cdot \mathcal{B}_{\omega\to3\pi}$	$2.3 \pm 0.7 \pm 0.2$	$1.1 \pm 0.3 \pm 0.1$	No entry
$\Gamma_{ee}^{\psi(2S)} \cdot \mathcal{B}_{\psi(2S)\to\rho^\pm\pi^\mp\pi^0\pi^0}$	<6.2 at 90% C.L.	<2.6 at 90% C.L.	No entry
$\Gamma_{ee}^{\psi(2S)} \cdot \mathcal{B}_{\psi(2S)\to\pi^+\pi^-\pi^0\pi^0\eta}$	<0.85 at 90% C.L.	<0.35 at 90% C.L.	No entry

VII. SUMMARY

The photon-energy and charged-particle momentum resolutions together with the particle identification capabilities of the *BABAR* detector permit the reconstruction of the $\pi^+\pi^-3\pi^0$ and $\pi^+\pi^-2\pi^0\eta$ final states produced at low effective center-of-mass energies via initial-state photon radiation in data collected in e^+e^- annihilation in the $\Upsilon(4S)$ mass region.

The analysis shows that the effective luminosity and efficiency have been understood with 10%–13% accuracy. The cross section measurements for the reaction $e^+e^- \to \pi^+\pi^-\pi^0\pi^0\pi^0$ present a significant improvement on existing data. The $e^+e^- \to \pi^+\pi^-\pi^0\pi^0\eta$ cross section has been measured for the first time.

The selected multihadronic final states in the broad range of accessible energies provide new information on hadron spectroscopy. The observed $e^+e^- \to \omega\pi^0\pi^0$ and $e^+e^- \to \eta\pi^+\pi^-$ cross sections provide evidence of resonant structures around 1.4 and 1.7 GeV/c^2, which were previously observed by DM2 and interpreted as $\omega(1450)$ and $\omega(1650)$ resonances.

The initial-state radiation events allow a study of J/ψ and $\psi(2S)$ production and a measurement of the corresponding products of the decay branching fractions and e^+e^- width for most of the studied channels, the majority of them for the first time.

ACKNOWLEDGMENTS

We are grateful for the extraordinary contributions of our PEP-II colleagues in achieving the excellent luminosity and machine conditions that have made this work possible. The success of this project also relies critically on the expertise and dedication of the computing organizations that support *BABAR*. The collaborating institutions wish to thank SLAC for its support and the kind hospitality extended to them. This work is supported by the U.S. Department of Energy and National Science Foundation, the Natural Sciences and Engineering Research Council (Canada), the Commissariat à l'Energie Atomique and Institut National de Physique Nucléaire et de Physique des Particules (France), the Bundesministerium für Bildung und Forschung and Deutsche Forschungsgemeinschaft (Germany), the Istituto Nazionale di Fisica Nucleare (Italy), the Foundation for Fundamental Research on Matter (Netherlands), the Research Council of Norway, the Ministry of Education and Science of the Russian Federation, Ministerio de Economía y Competitividad (Spain), the Science and Technology Facilities Council (United Kingdom), and the Binational Science Foundation (U.S.-Israel). Individuals have received support from the Marie-Curie IEF program (European Union) and the A. P. Sloan Foundation (USA).

[1] V. N. Baier and V. S. Fadin, Phys. Lett. **27B**, 223 (1968).
[2] A. B. Arbuzov, E. A. Kuraev, N. P. Merenkov, and L. Trentadue, J. High Energy Phys. 12 (1998) 009.
[3] S. Binner, J. H. Kühn, and K. Melnikov, Phys. Lett. B **459**, 279 (1999).
[4] M. Benayoun, S. I. Eidelman, V. N. Ivanchenko, and Z. K. Silagadze, Mod. Phys. Lett. A **14**, 2605 (1999).
[5] M. Davier, A. Hoecker, B. Malaescu, and Z. Zhang, Eur. Phys. J. C **77**, 827 (2017); F. Jegerlehner, EPJ Web Conf. **166**, 00022 (2018); A. Keshavarzi, D. Nomura, and T. Teubner, Phys. Rev. D **97**, 114025 (2018).
[6] B. Aubert *et al.* (*BABAR* Collaboration), Phys. Rev. D **69**, 011103 (2004).
[7] B. Aubert *et al.* (*BABAR* Collaboration), Phys. Rev. Lett. **103**, 231801 (2009); J. P. Lees *et al.* (*BABAR* Collaboration), Phys. Rev. D **86**, 032013 (2012).
[8] J. P. Lees *et al.* (*BABAR* Collaboration), Phys. Rev. D **88**, 032013 (2013).
[9] J. P. Lees *et al.* (*BABAR* Collaboration), Phys. Rev. D **88**, 072009 (2013).
[10] B. Aubert *et al.* (*BABAR* Collaboration), Phys. Rev. D **71**, 052001 (2005).
[11] B. Aubert *et al.* (*BABAR* Collaboration), Phys. Rev. D **86**, 012008 (2012).
[12] B. Aubert *et al.* (*BABAR* Collaboration), Phys. Rev. D **73**, 052003 (2006).
[13] B. Aubert *et al.* (*BABAR* Collaboration), Phys. Rev. D **70**, 072004 (2004).
[14] B. Aubert *et al.* (*BABAR* Collaboration), Phys. Rev. D **76**, 092005 (2007).
[15] J. P. Lees *et al.* (*BABAR* Collaboration), Phys. Rev. D **96**, 092007 (2017).
[16] B. Aubert *et al.* (*BABAR* Collaboration), Phys. Rev. D **77**, 092002 (2008).
[17] J. P. Lees *et al.* (*BABAR* Collaboration), Phys. Rev. D **89**, 092002 (2014).
[18] G. Cosme *et al.*, Nucl. Phys. **B152**, 215 (1979).
[19] B. Esposito *et al.*, Lett. Nuovo Cimento **25**, 5 (1979).
[20] J. P. Lees *et al.* (*BABAR* Collaboration), Phys. Rev. D **97**, 052007 (2018).
[21] J. P. Lees *et al.* (*BABAR* Collaboration), Nucl. Instrum. Methods Phys. Res., Sect. A **726**, 203 (2013).
[22] B. Aubert *et al.* (*BABAR* Collaboration), Nucl. Instrum. Methods Phys. Res., Sect. A **479**, 1 (2002); **729**, 615 (2013).
[23] H. Czyż and J. H. Kühn, Eur. Phys. J. C **18**, 497 (2001).
[24] A. B. Arbuzov, E. A. Kuraev, G. V. Fedotovich, N. P. Merenkov, V. D. Rushai, and L. Trentadue, J. High Energy Phys. 10 (1997) 001.
[25] M. Caffo, H. Czyż, and E. Remiddi, Nuovo Cim. A **110**, 515 (1997); Phys. Lett. B **327**, 369 (1994).
[26] E. Barberio, B. van Eijk, and Z. Was, Comput. Phys. Commun. **66**, 115 (1991).
[27] M. Tanabashi *et al.* (Particle Data Group), Phys. Rev. D **98**, 030001 (2018).
[28] S. Agostinelli *et al.* (GEANT Collaboration), Nucl. Instrum. Methods Phys. Res., Sect. A **506**, 250 (2003).
[29] T. Sjöstrand, Comput. Phys. Commun. **82**, 74 (1994).
[30] S. Jadach and Z. Was, Comput. Phys. Commun. **85**, 453 (1995).
[31] V. M. Aulchenko *et al.*, Phys. Rev. D **91**, 052013 (2015).
[32] M. N. Achasov *et al.* (SND Collaboration), Phys. Rev. D **94**, 032010 (2016).
[33] J. E. Augustin *et al.* (DM2 Collaboration), Nucl. Phys. **B320**, 1 (1989).